218600-4-F

(2)

SIMULTANEOUS ACTIVE AND PASSIVE MICROWAVE MEASUREMENTS OF THE OCEAN SURFACE

R. G. Onstott
R. A. Shuchman
C. L. Rufenach
Advanced Concepts Division
Center for Earth Sciences

JUNE 1991

Technical Monitor: Dr. Frank Herr
Office of Naval Research
800 N. Quincy Street
Arlington, VA 22217

Contract No: N00014-89-C-0117

ERIM
P.O. Box 134001
Ann Arbor, MI 48113-4001

REPORT DOCUMENTATION PAGE

Form Approved
OMB No. 0704-0188

1. AGENCY USE ONLY (Leave blank)	2. REPORT DATE	3. REPORT TYPE AND DATES COVERED
	June 1991	Final Report 8/1/89 - 6/30/91

4. TITLE AND SUBTITLE
Simultaneous Active and Passive Microwave Measurements of the Ocean

5. FUNDING NUMBERS
N00014-89-C-0117

6. AUTHOR(S) R.G. Onstott
R.A. Shuchman
C.L. Rufenach

7. PERFORMING ORGANIZATION NAME(S) AND ADDRESS(ES)
Environmental Research Institute
of Michigan (ERIM)
P.O. 134001
Ann Arbor, MI 48113-4001

8. PERFORMING ORGANIZATION REPORT NUMBER
218600-4-F

9. SPONSORING/MONITORING AGENCY NAME(S) AND ADDRESS(ES)
Office of Naval Research (ONR)
800 N. Quincy Street
Arlington, VA 22217-5000

10. SPONSORING/MONITORING AGENCY REPORT NUMBER

11. SUPPLEMENTARY NOTES

12a. DISTRIBUTION/AVAILABILITY STATEMENT

12b. DISTRIBUTION CODE

13. ABSTRACT *(Maximum 200 words)*

This report considered both the use of an L- and X-band scatterometer to measure surface slicks on the ocean as well as the feasibility of using a dual linear-polarized radiometer operating at 6 GHz in conjunction with a scatterometer to measure sea surface temperature.

The scatterometer measurements show: (1) the largest peaks in florescence, a measure of the peak Chlorophyll A concentration, are co-located with the short wave damping at 24 cm and the 4 cm wavelengths, (2) the maximum damping ratio, between the 24 cm and 4 cm waves, is at least 16 for wind speeds, 3-4 m/s, and (3) the radar roughness signatures at these short Bragg gravity wavelengths suggest the slicks are caused by damping rather than straining of these waves. Additional shipboard measurements are needed to further quantify these preliminary results.

The active/passive microwave feasibility study indicated a $\pm$ .12° c accuracy of SST can result if a scatterometer is used to correct the wind speed dependence of a vertically polarized radiometer operating near 6 GHz using a pencil antenna beam pointing at an incidence angle near 55°.

14. SUBJECT TERMS

15. NUMBER OF PAGES
106

16. PRICE CODE

17. SECURITY CLASSIFICATION OF REPORT	18. SECURITY CLASSIFICATION OF THIS PAGE	19. SECURITY CLASSIFICATION OF ABSTRACT	20. LIMITATION OF ABSTRACT
Unclassified	Unclassified	Unclassified	Unlimited

GENERAL INSTRUCTIONS FOR COMPLETING SF 298

The Report Documentation Page (RDP) is used in announcing and cataloging reports. It is important that this information be consistent with the rest of the report, particularly the cover and title page. Instructions for filling in each block of the form follow. It is important to ***stay within the lines*** to meet ***optical scanning requirements***.

Block 1. Agency Use Only *(Leave blank)*.

Block 2. Report Date. Full publication date including day, month, and year, if available (e.g. 1 Jan 88). Must cite at least the year.

Block 3. Type of Report and Dates Covered. State whether report is interim, final, etc. If applicable, enter inclusive report dates (e.g. 10 Jun 87 - 30 Jun 88).

Block 4. Title and Subtitle. A title is taken from the part of the report that provides the most meaningful and complete information. When a report is prepared in more than one volume, repeat the primary title, add volume number, and include subtitle for the specific volume. On classified documents enter the title classification in parentheses.

Block 5. Funding Numbers. To include contract and grant numbers; may include program element number(s), project number(s), task number(s), and work unit number(s). Use the following labels:

C	- Contract	PR	- Project
G	- Grant	TA	- Task
PE	- Program Element	WU	- Work Unit Accession No.

Block 6. Author(s). Name(s) of person(s) responsible for writing the report, performing the research, or credited with the content of the report. If editor or compiler, this should follow the name(s).

Block 7. Performing Organization Name(s) and Address(es). Self-explanatory.

Block 8. Performing Organization Report Number. Enter the unique alphanumeric report number(s) assigned by the organization performing the report.

Block 9. Sponsoring/Monitoring Agency Name(s) and Address(es). Self-explanatory.

Block 10. Sponsoring/Monitoring Agency Report Number. *(If known)*

Block 11. Supplementary Notes. Enter information not included elsewhere such as: Prepared in cooperation with...; Trans. of...; To be published in.... When a report is revised, include a statement whether the new report supersedes or supplements the older report.

Block 12a. Distribution/Availability Statement. Denotes public availability or limitations. Cite any availability to the public. Enter additional limitations or special markings in all capitals (e.g. NOFORN, REL, ITAR).

- DOD - See DoDD 5230.24, "Distribution Statements on Technical Documents."
- DOE - See authorities.
- NASA - See Handbook NHB 2200.2.
- NTIS - Leave blank.

Block 12b. Distribution Code.

- DOD - Leave blank.
- DOE - Enter DOE distribution categories from the Standard Distribution for Unclassified Scientific and Technical Reports.
- NASA - Leave blank.
- NTIS - Leave blank.

Block 13. Abstract. Include a brief *(Maximum 200 words)* factual summary of the most significant information contained in the report.

Block 14. Subject Terms. Keywords or phrases identifying major subjects in the report.

Block 15. Number of Pages. Enter the total number of pages.

Block 16. Price Code. Enter appropriate price code *(NTIS only)*.

Blocks 17. - 19. Security Classifications. Self-explanatory. Enter U.S. Security Classification in accordance with U.S. Security Regulations (i.e., UNCLASSIFIED). If form contains classified information, stamp classification on the top and bottom of the page.

Block 20. Limitation of Abstract. This block must be completed to assign a limitation to the abstract. Enter either UL (unlimited) or SAR (same as report). An entry in this block is necessary if the abstract is to be limited. If blank, the abstract is assumed to be unlimited.

PREFACE

This report summarizes the activities supported under the Office of Naval Research (ONR) Contract No. N00014-89-C-0117. The ONR technical monitor for the activity was Dr. Frank Herr. The ERIM principal investigator was Dr. Robert Shuchman. Dr. Robert Onstott and Mr. Scott Gaboury collected the active and passive microwave data during SLICKEX, while Dr. Clifford Rufenach and Dr. Robert Shuchman aided Dr. Robert Onstott in the analysis and interpretation of the data.

CONTENTS

LIST OF FIGURES vii
LIST OF TABLES ix
1.0 EXECUTIVE SUMMARY 1
2.0 INTRODUCTION 3
3.0 SLIX '89 EXPERIMENTAL DESCRIPTION 6
3.1 MEASUREMENTS 8
3.2 BRAGG SCATTERING MODEL 17
3.3 OCEAN SLICK RESULTS 21
3.4 EOM MODEL 30
4.0 RADIOMETRIC MODEL 33
4.1 SEA SURFACE TEMPERATURE RESULTS 35
5.0 PROPOSED FURTHER ANALYSIS AND FUTURE EXPERIMENTS 44
5.1 RECOMMENDED ADDITIONAL ANALYSIS OF SLIX '89 44
5.2 PROPOSED FUTURE EXPERIMENTS 44
6.0 SUMMARY 46
7.0 BIBLIOGRAPHY 47
APPENDIX: PUBLICATIONS RESULTING FROM THIS RESEARCH 51

FIGURES

1. (a) Artists rendition of the research vessel Wecoma relative to towed catamaran (SCUMS) (b) Side view of the catamaran and attached SCUMS sampler 9

2. Photograph of the radio microwave sensors: radar scatterometers and passive radiometers 11

3. Stacked plots of measured parameters for the 40 min period 10:40 to 11:20 PDT for two slick wave groups from R/V Wecoma, morning of October 16, 1989 14

4. Plan view of ship track and areas of surface slick group on the R/V Wecoma on October 16, 1989 15

5. Stacked plots of measured parameters for the 40 min period 10:40 to 11:20 PDT similar to Figure 4 22

6. Synthetic aperture radar image of internal wave slicks in the Georgia Straits . . 25

7. The exponential decay time for both the free surface and the inextensible microlayer as a function of Bragg wavelength between 4 cm and 24 cm 29

8. EOM radar cross section variation as a function of film pressure π for vertical transmit and receive polarization at an incidence angle of 25° 31

9. Emissivity variation with sea surface temperature based on a smooth sea parameterized in salinity at normal incidence using: (a) radiometric frequency of 6 GHz (C-Band), and (b) radiometric frequency of 2.65 GHz (S-Band) 38

10. Emissivity variation with incidence angle parameterized in surface wind speed, 6 m/s, 10 m/s and 20 m/s 40

11. Emissivity variation with sea surface temperature parameterized in surface wind speed, 6 - 20 m/s, incidence angle = 60° and salinity = 34 ppt; (a) horizontal polarization, and (b) vertical polarization 42

TABLES

1. Scatterometer and radiometer system parameters 7

2. Bragg wavelength for L-band and X-band radar at $\theta = 25°$ 18

3. Wind speed and associated percent effective foam cover based on Wilheit's model 37

4. Radiometric brightness temperature sensitivity to: (a) salinity at normal incidence, (b) radiometric brightness temperature sensitivity to wind speed, s = 34 ppt and $\theta = 60°$ 39

1.0 EXECUTIVE SUMMARY

We measured the radar backscattered cross section across naturally occurring ocean slicks during SLIX '89 and also developed expressions for the sensitivity of active/passive sensors for extracting sea surface temperature.

The results include ship-based radar scatterometer measurements at L-band and X-band and microlayer chlorophyll fluorescence measurements on the southern California continental shelf across several surface slicks during October, 1989. These measurements allowed the simultaneous extraction of both the short wave damping at Bragg wavelengths of 24 cm and 4 cm and the chlorophyll A biological concentration with sufficient spatial resolution to observe features within individual slick bands.

The measurements show: (1) the largest peaks in fluorescence, a measure of the peak Chlorophyll A concentration, are co-located with the short wave damping at 24 cm and 4 cm wavelengths, (2) the maximum damping ratio, between the 24 cm and 4 cm waves is at least 16 for wind speeds, 3-4 m/s, and (3) the radar roughness signatures at these short Bragg gravity wavelengths suggest the slicks are caused by damping rather than straining of these waves. Additional shipboard measurements are needed to further quantify these preliminary results.

We study the feasibility of using a dual linear-polarized radiometer operating at 6 GHz in conjunction with a scatterometer as a method of extracting sea surface temperature. A model originally developed by Wilheit [1979] is used to investigate the sensitivity of radiometric temperature to changes in wind speed, U, at a height of 20 m; that is, the sea temperature accuracy depends directly on the radiometric temperature accuracy. These changes are corrected using this extracted wind speed based on a scatterometer wind accuracy of $\pm$ 1 m/s. We show, as previously reported, that a vertically polarized radiometer is less sensitive to wind speed changes than a horizontally polarized one near an incidence angle $\Theta = 60°$. Furthermore, we

quantify the wind variation; $\Delta T_B^V/\Delta U \lesssim 0.12°C/m/s$ when $U > 10$ m/s and $\Delta T_B^H/\Delta U \lesssim 2.0°C/m/s$ when $U > 6$ m/s for vertical and horizontal polarization, respectively. Thus, the resulting error is $\pm$ 0.12°C and $\pm$ 2.0°C for T_B^V and T_B^H based on the extracted wind accuracy $\pm$ 1 m/s. These results suggest that a scatterometer can be used to correct the wind speed dependence of a vertically polarized radiometer operating near 6 GHz using a pencil antenna beam pointing at an incidence angle near 55°.

A number of symposium and referred journal articles have resulted from this research effort. Table 1 lists these articles, while the appendix of this report provide a copy of each.

2.0. INTRODUCTION

Numerous active (scatterometric) and passive (radiometric) microwave measurements of the ocean surface have been acquired, analyzed and interpreted over the last twenty years. However, few simultaneous active and passive measurements have been interpreted in terms of physical properties of the ocean surface. Simultaneous measurements have the potential of extracting sea surface temperature more accurately than passive measurements alone. Furthermore, simultaneous shipboard microwave measurements in conjunction with the Self Contained Underway Microlayer Sampler (SCUMS) towed from the side of a ship [Carlson et al., 1988] during the Marine Microlayer Slick Experiment (SLIX '89) produced information about the concentration of the marine microlayer material and associated damping of the short gravity waves within individual ocean slick bands.

The radiometric temperature of an ocean surface depends primarily upon its sea surface temperature, salinity, surface wind speed (surface roughness), and foam cover. A smooth surface does not depend on the wind speed or foam cover; indeed, foam cover is not important for wind speeds less than about 7 m/s. A smooth sea surface depends on surface temperature and salinity. This dependence is known accurately through its relationship with the complex dielectric constant of sea water [Klein and Swift, 1977]. The surface wind influences the radiometric temperature through the ocean wave spectrum. However, measurements are not fully consistent with each other or with the theory especially when foam is present [Hollinger, 1971 and Swift, 1974]. Additional surface based measurements are required to validate radiometric models before additional aircraft and/or spacecraft based measurements can be fully interpreted.

Radar scatterometers measure the ocean surface roughness at Bragg wavelengths, 3 cm - 30 cm, within the radar's antenna beamwidth. The SCUMS platform contains Fluorescence and UV absorbance detectors. Fluorescence detectors measure the

concentration of the biological material, chlorophyll A; whereas, the UV absorbance detectors (280 nm) measure the concentration of chemical material. The ability of the microlayer to dampen short waves increases with the concentration of the microlayer material. This concentration varies across slicks due to the horizontal convergence of ocean currents at the surface and/or by horizontal convergence due to wind stress. That is, the surface roughness near and within slick bands vary with ocean current and wind.

Slicks on the southern California and Baja continental shelf can be due to internal waves currents, small scale ocean circulation and wind stress. The internal waves typically travel along the thermocline at the same speed as the companion slick bands. These slicks are characterized by a series of slick packets; each packet separated by a distance of 15 - 20 km with an envelope of quasi-period parallel slick bands with wavelengths of about 300 m [Ewing, 1950; and Apel and Gonzalez, 1983].

The slick characteristics can be used to distinguish internal wave generated slicks from other slick generating mechanisms. The surface roughness at short gravity wavelengths associated with quasi-periodic slicks have been observed by a number of workers using different measuring methods; see, e. g., Ewing [1950], LaFond [1962], Rufenach and Smith [1985], Alpers [1985], Shuchman et al. [1988], Lyzenga and Bennett [1988] and Gasparovic et al. [1988]. Alternating bright and dark bands in radar images have been interpreted as horizontal current gradients produced by internal waves; see, e. g., Alpers [1985]; or equivalently, increases and decreases in radar cross section (RCS). In contrast, RCS decreases are directly related to the damping of these short waves due to increases in the concentration of the surface marine microlayer material. Surface roughness changes have usually been interpreted in terms of either damping or straining of the short waves but not both. We believe that both mechanisms may be important on some occasions.

The concentration of the surface microlayer material has been related to the bulk viscosity [Carlson, 1982; Carlson, 1987]. Microlayer viscous damping is caused by either

the bulk viscosity, syrupy nature of the surface layer, or the elasticity, visco-elastic nature of this thin surface layer. The elastic properties are equivalent to an additional viscosity of the surface microlayer [Levich, 1962]. We do not attempt to distinguish between these two viscous damping mechanisms.

Detection of bands of slicks associated with internal waves by passive microwave sensors have not been reported. Passive microwave sensors have been primarily operated from spaceborne platforms with a spatial resolution $\gtrsim$ 20 km. This resolution could explain the lack of detection since the slick packet spacing is typically 10 - 15 km. Increases in emissivity have been measured across man made oil slicks by microwave sensors [Hollinger and Mannella, 1973] whereas one example of a large emissitivity decrease has been reported across a manmade monomolecular slick [Hühnerfuss and Alpers, 1983]. Additional shipboard multi-frequency active and passive microwave measurements in conjunction with in situ measurements across manmade and natural slicks are needed to better understand the radio perturbations caused by surface slicks

This report is limited to determining an optimum radiometric frequency for the measurement of sea surface temperature using an active/passive sensor system and the comparison of scatterometer and radiometer measurements with in situ fluorescence measurements near two surface slick groups off the California coast.

3.0. SLIX '89 EXPERIMENTAL DESCRIPTION

The ship-board SLIX '89 designed to traverse surface slicks off the coast of southern California near San Diego during a two week period in October 1989. The ship heading during the experiment was selected to intersect slick groups visually observed from the bridge of the ship. This experiment included a variety of in situ and remote sensing instruments including the microwave sensors and SCUMS catamaran in situ detectors.

The microwave sensors were mounted about 10 m above the sea surface toward the bow of the ship, R/V Wecoma, whereas the in situ instruments were towed by a catamaran attached to a boom on the port side of the ship. The wind velocity at a height of about 10 m was measured near the bow of the ship and sea surface temperature was measured at a depth of 15 cm. We operated the following microwave sensors:

(1) a dual wavelength radar scatterometer, and

(2) a dual wavelength radiometer,

both mounted on the port side with their antennas pointing perpendicular to the ship's track. The radar operating wavelengths were L-band and X-band (20 cm and 3.2 cm) while the radiometers operated at C-band and Ka-band wavelengths (5.5 cm and 0.86 cm). The radiometer outputs were carefully monitored for interference from the scatterometer. The relevant instrument parameters are given in Table 1. The radiometers were calibrated using a hot absorber and cold (near zenith sky scan) load.

The in situ measurements of interest were taken on board the catamaran towed about 20 m aft of the microwave sensors from the port side of the ship, SCUMS [Carlson et al., 1988]. The UV absorbance is related to the concentration of the absorbing organic

TABLE 1.

Scatterometer and Radiometer System Parameters

	RADAR	RADIOMETER		
FREQUENCY	1.5 GHz	9.38 GHz	5.4 GHz	35 GHZ
WAVELENGTH	20 cm	3.2 cm	5.5 cm	0.86 cm
ANTENNA SPOT SIZE at Θ = 55° at Θ = 25° §	 3.7 m 1.5 m	 1.3 m 0.5 m	 5.3 m 2.1 m	 5.3 m 2.1 m
INTEGRATION TIME	50 sec	50 sec	50 sec	50 sec
BANDWIDTH	350 MHz	575 MHz	70 MHz	500 MHz
POLARIZATION	HH,VV or VH	HH,VV or VH	H or V	H or V
RESOLUTION	1.1 dB	2.6 dB	0.21°K	0.12°K
ABSOLUTE ACCURACY	± 1 dB	± 1 dB	± 1°K	± 1°K

* H signifies horizontal polarization and V signifies vertical polarization.

§ incidence angle used during measurements across slick groups "A" and "B" on October 16.

molecules, whereas the chlorophyll A fluorescence is related to the concentration of the biota. The SCUMS measurements include: the fluorescence and the UV absorption measured in both the microlayer and sub-layer. The microlayer material was attached to a rotating drum then skimmed from the drum surface whereas the sub-surface material was collected at a depth of about 15 cm. The microlayer is thought to be 50-100 μm thick. The fluorescence and UV absorbance show similar variations across the slicks implying that the concentration of the surface microlayer material can be represented to first order by either detector.

A side view of the ship, catamaran and remote sensing instruments are shown in Figure 1(a) and a side view of the catamaran and associated instrumentation is shown in Figure 1(b). A photograph of the microwave antennas are given in Figure 2. Selected measurements during SLIX '89 are given in the following section.

3.1 MEASUREMENTS

Two surface slick groups off the coast of San Diego during October 16 were selected for analysis. These two groups each exhibit three slick bands during a period when both the microwave and in situ instruments were operating. Furthermore, these two slick groups were visually observed from the ship deck as recorded in the operational log. We distinguish between groups and packets in the present work: packets are associated with internal waves; typically separated by 15 - 20 km. Groups are more closely spaced clusters of slick bands, several occurring within a packet, due to the complex nature of the bands or generating mechanisms other than internal waves. The orientation of these slick bands relative to the radar look direction is not known since radar imagery was not available and no orientation information was recorded in the log. However, the experiment objective was to traverse the slick bands. That is, the fluorescence and radar measurements show a fluctuating component along the ship track.

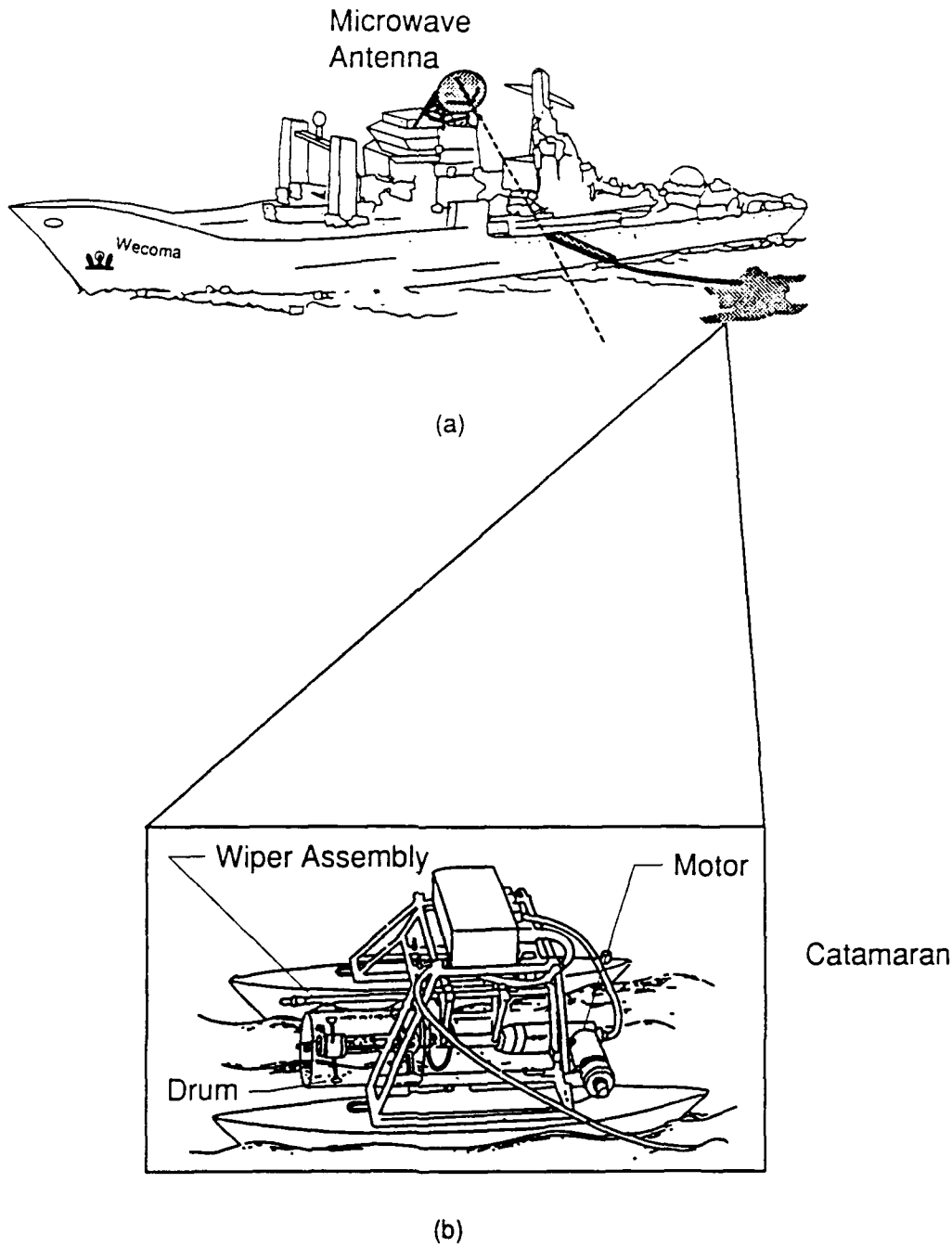

91-20063

Figure 1. (a) Artists Rendition of the Research Vessel Wecoma Relative to Towed Catamaran (SCUMS). The Microwave Equipment Measures Radar Cross Section (RCS) and Radiometric Brightness Temperature. The SCUMS Instrument Measures Fluorescence and UV Absorbance of the Surface Layer Organic Material. (b) Side View of the Catamaran and Attached SCUMS Sampler. The Micro-Layer Film Attaches Itself to the Rotating Cylindrical Mirror Surfaced Drum. The Microlayer Material is Extracted From the Drum and Pumped Into the Ship Where it is Analyzed.

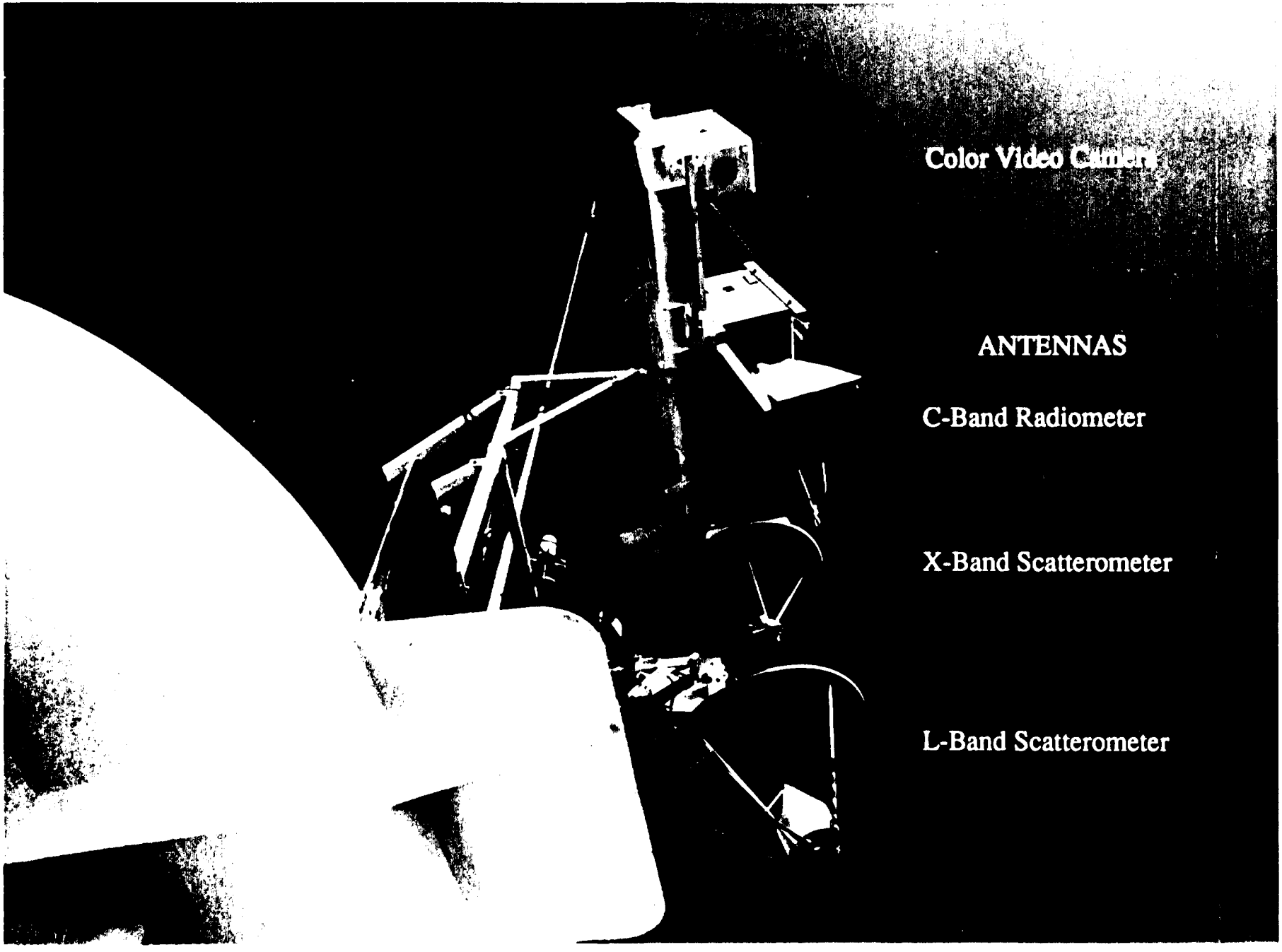

Figure 2. Photograph of the Radio Microwave Sensors: Radar Scatterometers and Passive Radiometers.

We have no direct measurements in the water column that these slicks were produced by internal waves or any other mechanism. However, the separation between the two groups ($\approx$ 30 min.) and a slick band spacing (3 - 5 min.), see Figure 3, suggest spatial separations; the order of a few km and hundreds of meters, respectively. The 3 - 5 min. quasi-periodic spacing are consistent with internal wave produced slick bands provided the ship speed (0.5 - 1 m/s) is much larger than that component of the slick velocity along the ship track. The spatial separation of a few kilometers suggest that the two slick groups are not internal wave associated packets. The grey areas depicted in Figure 4 give the location of the two slick groups relative to the ship track during October 16. The two slick groups occurred in the morning hours between 10:40 to 11:20 Pacific Daylight Time (PDT). There were no clouds or rain during this period.

An overview of the microwave and in situ measurements using stacked plots of the various parameters is given in Figure 4. The measured parameters (1 min averages) are displayed on the ordinate and the time in minutes is displayed on the abscissa in all the plots. The values of RCS (σ^o), fluorescence relative to the sub-layer (F_r) and radiometric brightness temperature (T_B) were selected for display. The two σ^o's at L-band and X-band are indicated in Figure 4(a). The relative slick fluorescence (F_r) is obtained by dividing the microlayer fluorescence by the sub-layer fluorescence. The inherent delay in skimming and pumping the surfactant microlayer has been corrected. The delay due to the spatial separation of the microwave instruments and the catamaran, $\lesssim$ 20 sec, has not been corrected. The radiometric brightness temperatures at C-band and Ka-band show no discernible change across the slick bands. That is, any surface slope decrease due to the slicks was not detected by these radiometers.

The UV absorbance and the fluorescence show similar variations across the two surface slick groups of October 16. We select the fluorescence for detailed analysis in the present work. The fluorescence changes from 10:40 to 11:20 is a measure of the concentration of the chlorophyll A within the two slick groups separated by a relatively

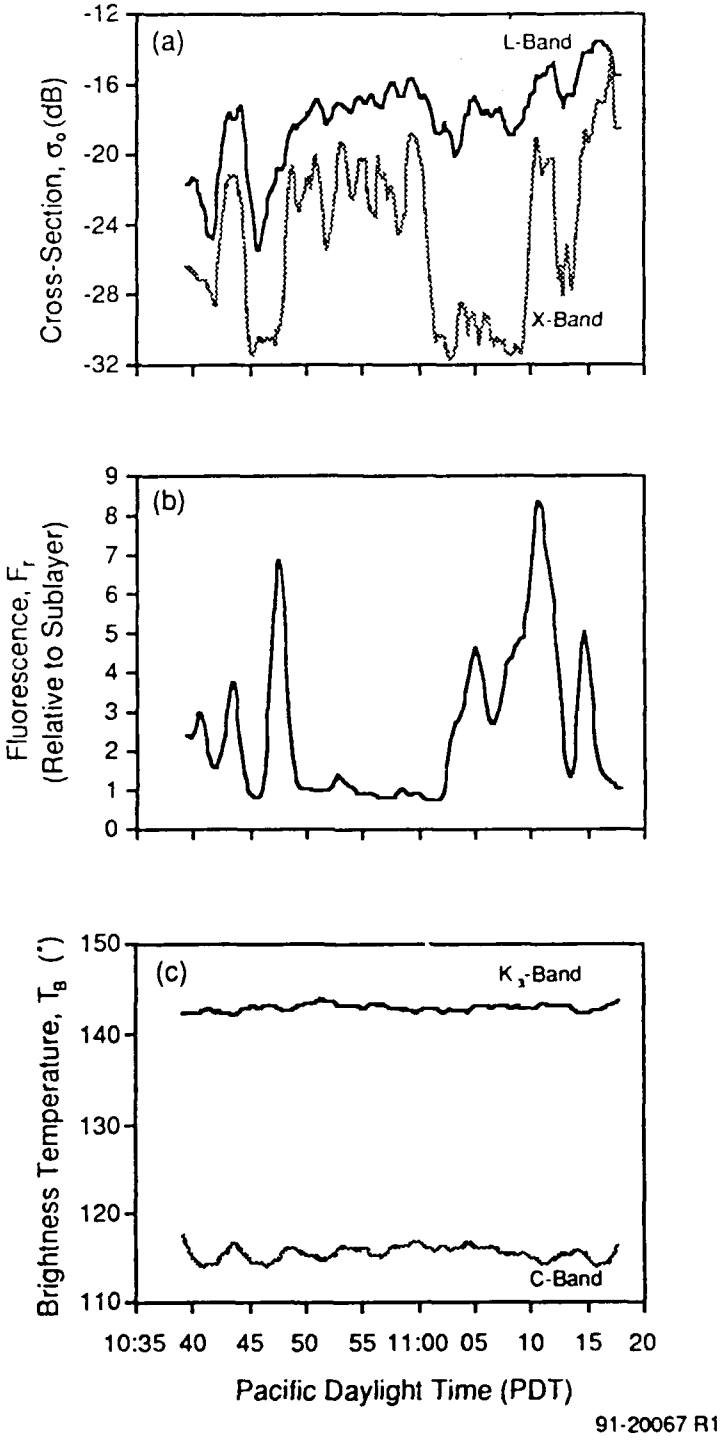

Figure 3. Stacked Plots of Measured Parameters for the 40 Minute Period 10:40 to 11:20 PDT for Two Slick Wave Groups From R/V Wecoma, Morning of October 16, 1989. The Measured Parameters are: (a) Radar Backscatter Cross Section (σ^o), (b) Slick Fluorescence Relative to the Sub-Layer (F_r) and (c) Radiometric Brightness Temperature (T_B). The Polarization was Vertical for the Radiometer and Horizontal Transmit and Horizontal Receive for the Radar Both at an Incidence Angle of $\Theta = 25°$.

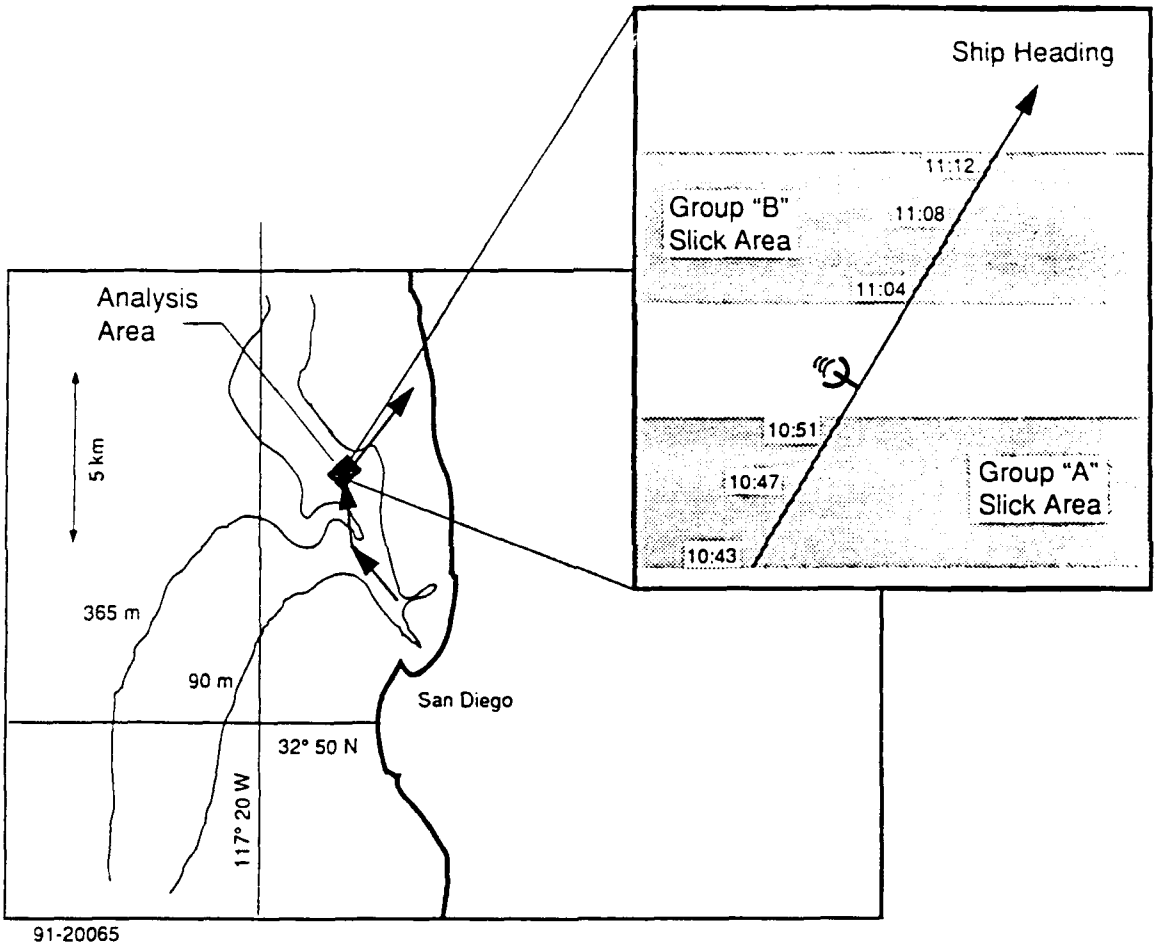

Figure 4. Plan View of Ship Track and Areas of Surface Slick Group on the R/V Wecoma on October 16, 1989. The Ocean Depth is Indicated by the Contours 90 m and 365 m.

surfactant free region. The first group is designated as group "A" and the second group is designated as group "B". The three peaks in fluorescence F_r within each slick group are interpreted as three slick bands.

The relative fluorescence F_r increased to a peak value of 7 within the slick group "A" near 10:47. The radar cross section also decreased about 10 dB at X-band and 6 dB at L-band, both near 10:47, co-located with the fluorescence peak. This co-location is direct evidence that the short Bragg waves are damped at the peak surfactant concentration near the center of the slick band.

The relative fluorescence F_r increased to a peak value of 8 within slick group "B" near 11:10. Different RCS decreases are apparent within slick group "B" compared to slick group "A". The RCS decreased about 10 dB at X-band similar to slick group "A" whereas the cross section decreased about 2 dB at L-band in contrast to the 6 dB decrease in slick group "A". Furthermore, the X-band decrease occurred over a longer interval, about 8 min, than group "A". This large damping at X-band, reducing the backscattered energy to near the noise floor of the scatterometer, does not allow co-location of the peak fluorescence F_r with the radar minima signatures. That is, this X-band damping occurred across several slick bands within Group "B", whereas, the L-band radar minima are approximately co-located with all three fluorescence peaks.

The wind speed changed from about 1.5 m/s to about 4 m/s while the wind direction changed from about 60° to about 30° with respect to the radar look direction from group "A" to group "B". The wind was blowing generally toward the south and south-east toward the radar look direction. The ship speed was about 0.5 m/s. The wind speeds were light, 1.5-3 m/s inside group "A" at a wind direction of about 60°. Slightly higher wind speeds, 3-4 m/s were observed inside group "B" at a direction of about 30°. The differences between the X-band RCS decreases within the two slick groups could be due to the wind direction changes between the two slick groups. These differences are discussed in more detail in the following sections. Decreases in RCS co-located with

fluorescence peaks were also observed within several other slicks.

3.2 BRAGG SCATTERING MODEL

Typical ocean remote sensing radars operate at microwave wavelengths in the centimeter or decimeter range at incidence angles, Θ from 20-70° within which the radar backscatter is dominated by Bragg scattering. The RCS to first order for horizontal transmit and receive polarization is given by [Valenzuela, 1978],

$$\sigma^0(k_b) = 4\, k_0^4 \cos^4 \Theta \;\; | \, g_{HH}(\Theta) \, |^2 \, S(k_b,0) \qquad \text{(Eq. 1)}$$

where k_0 is the radar wavenumber, $S(k_x,k_y)$ is the spectral density of the ocean surface waves in rectangular coordinates, and $g_{HH}(\Theta)$ is the first order scattering coefficient dependent on the relative dielectric constant ϵ_r of the scattering surface,

$$g_{HH}(\Theta) = (\epsilon_r - 1)[\cos \Theta + (\epsilon_r - \sin \Theta)^{1/2}]^{-2} \qquad \text{(Eq. 2)}$$

the coordinate system is chosen such that the k_x is in the same plane as the radar antenna look direction and the internal wave travel direction. Equation (1) can then be used to estimate the ocean wave spectral density at the Bragg wavenumber, k_b, using

$$k_b = 2\, k_0 \sin \Theta \qquad \text{(Eq. 3)}$$

Indeed, the cross section measurements show decreases up to 6 dB and 10 dB at L-band and X-band due to damping of the wave spectral energy at the Bragg wavelengths within the slicks. The Bragg wavenumbers and wavelengths based on the radar configuration used during the October 16 morning measurements are given in Table 2. The RCS is

TABLE 2.

Bragg Wavelength for L-Band and X-Band Radar at $\theta = 25°$

	L-BAND	X-BAND
k_o	0.314 rad/cm	1.96 rad/cm
k_b	0.26 rad/cm	1.7 rad/cm
λ_b	23.7 cm	3.8 cm
ω_b §	16 rad/s	40 rad/s
f_b	2.5 Hz	6.4 Hz

§ ω_b is the intrinsic angular frequency of the Bragg wave.

proportional to the ocean wave spectral density at Bragg wavelengths 24 cm (L-band) and 4 cm (X-band). The relative attenuation of 24 cm waves compared to 4 cm waves can be estimated by forming the ratio of the L-band cross section $\sigma_L^0(k_b)$ to the X-band cross section $\sigma_X^0(k_b)$ as,

$$\sigma^0(k_{bL})/\sigma^0(k_{bX}) = \mid g^L_{HH}(\Theta) \mid^2 S(k_{bL},0)/ \mid g^X_{HH}(\Theta) \mid^2 S(k_{bX},0) \qquad \text{(Eq. 4)}$$

It can be shown that the ratio $\mid g^L_{HH}(\Theta) \mid^2 / \mid g^X_{HH}(\Theta) \mid^2 \approx 1$ when the imaginary part of ϵ_r, Im $\mid \epsilon_r \mid \gg 1$. We contend that this approximation applies to the surfactant free and surfactant covered ocean when $\Theta = 25°$ based on $\epsilon_r \approx 73 - 85i$ (L-band) and $\epsilon_r \approx 48 - 35i$ (X-band). That is, the skin depth (electromagnetic penetration depth) is large compared to the surfactant microlayer thickness. Indeed, the skin depth of sea water is about 1 cm and 0.2 cm at L-band and X-band, respectively, whereas the surfactant microlayer thickness is considered less than 0.1 cm. Therefore the scattering coefficient $g_{HH}(\Theta)$ should not be substantially effected by this microlayer film. Based on this result, we approximate equation (4) by,

$$\sigma^0(k_{bL})/\sigma^0(k_{bX}) \approx S(k_{bL},0)/ S(k_{bX},0) \qquad \text{(Eq. 5)}$$

The straining of the short Bragg waves by the internal waves can also be inferred using Bragg scattering theory. The normalized differential cross section $\delta\sigma^0/\sigma^0$ is proportional to the product of the internal wave horizontal-surface strain rate du/dx and the relaxation time τ_r [Alpers, 1985], given by,

$$\delta\sigma^0/\sigma^0 = -(4+\gamma)\, \tau_r\, du/dx \qquad \text{(Eq. 6)}$$

where γ is the ratio between the group and phase velocities (0.5 for gravity waves) of

the Bragg wave. The relaxation time depends on the radar look direction relative to the wind speed and direction, whereas the strain rate is dependent on the internal wave propagation direction and associated surface current gradient also relative to the radar look direction. The relaxation time is approximately equal to the reciprocal wind wave growth rate when the wind and waves are traveling in the same direction [Plant, 1982]

$$\tau_r = \beta^{-1} \approx 25\ (u_*/c)^{-2} / \omega \qquad \text{(Eq. 7)}$$

where u_* is the friction velocity (about 1/25 of the wind speed at 10 m height), c is the phase velocity and ω is the angular frequency of the surface waves. Equation (7) is, to first order, valid for a clean surface as demonstrated by Plant and a surfactant surface as demonstrated by Mitsuyasu and Honda [1986]. Alpers [1985] has estimated $\tau_r \approx 39$ sec for L-band Bragg waves at a wind speed of 4 m/s and internal wave strain rates in coastal regions of $du/dx \approx 10^{-3}$ sec^{-1}. However, the relaxation times based on equation (7) are much smaller at shorter wavelengths, $\tau_r \approx 1.6$ sec at X-band (4 cm) for similar wind speeds. Therefore the predicted changes in the surfactant free surface spectrum at 4 cm wavelengths is a factor of ~ 25 less than the L-band modulation (24 cm). The above parameters give,

$$\delta\sigma^0/\sigma^0 \sim 18\ \% \quad \text{at L-band} \qquad \text{(Eq. 8)}$$

$$\delta\sigma^0/\sigma^0 \sim 0.7\ \% \quad \text{at X-band.} \qquad \text{(Eq. 9)}$$

Indeed, the cross sectional modulation due to straining of the short waves is significantly smaller at X-band than L-band backscatter. More importantly, the radar signature due to straining has been observed as a series of bright and dark bands in radar imagery.

Equations (1) and (5) provide a method of extracting the damping of 24 cm and

4 cm ocean surface waves and their differential damping within a slick band. In contrast, equation (6) gives a method of extracting the product of the surface straining rate and the relaxation time. Furthermore, equation (6) is consistent with the bright/dark bands observed in radar imagery due to change in sign of du/dx. These expressions, equations (1) and (6), can be used to distinguish between cross sectional radar (reflectivity) modulation due to short wave damping and straining.

3.3. OCEAN SLICK RESULTS

We investigate the slick related parameters for the period 10:40-11:20 on October 16 in more detail. Stacked plots of selected parameters in Figure 5 are displayed in a format similar to Figure 4. The cross section in Figure 5 (a) is given in linear units, rather than logarithmic (dB) units, $\sigma^0_{dB}(k_b) = 10 \log \sigma^0(k_b)$. The ratio of the L-band to X-band cross section is given in Figure 5 (b). The cross sectional ratio is directly related to the ratio of the spectral densities at the 24 and 4 cm wavelengths, $S(k_{bL},0)/ S(k_{bX},0)$, see equation (5). The relative fluorescence F_r, originally displayed in Figure 4 (c) is also given in Figure 5.

These limited measurements of surface slicks show several interesting features. The relative fluorescence F_r is directly related to the concentration of the chlorophyll A within the slick bands. The ratio of 24 cm spectral damping to 4 cm damping is the largest within slick group "B". We investigated why the L-band cross section shows a greater backscatter decrease within group "A" compared to group "B". The wind direction changed from 60° relative to the radar look direction in group "A" to 30° in group "B", whereas, the wind speed increased about 1.5 m/s from about 2 m/s to about 3.5 m/s from group "A" to group "B". The individual slick band orientations are not known but are considered constant relative to the radar for the two slick groups. The sea surface temperature measured at 15 cm depth increased about 0.1° C from 18.8°C to

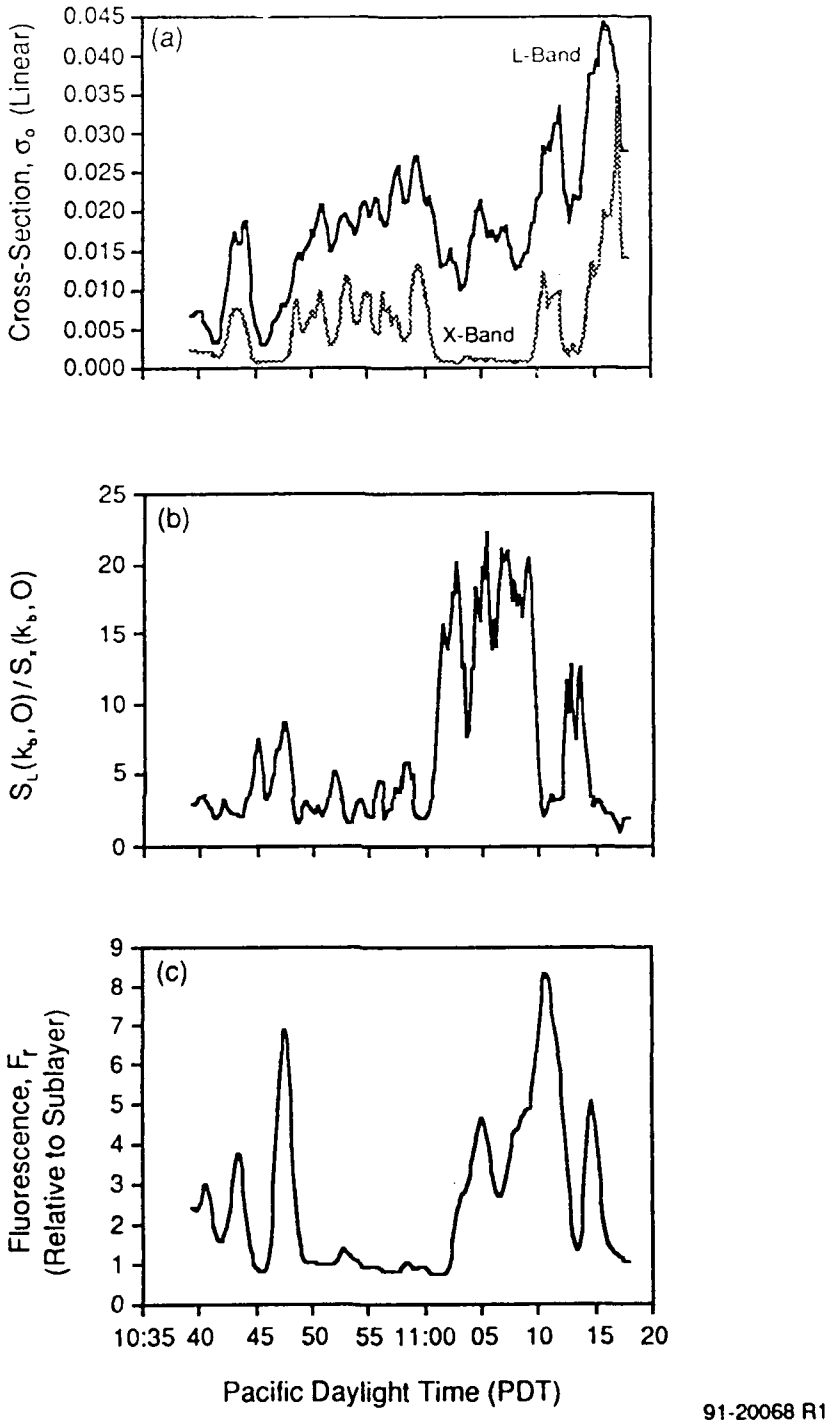

Figure 5. Stacked Plots of Measured Parameters for the 40 Minute Period 10:40 to 11:20 PDT Similar to Figure 4. The Measured Parameters are: (a) Radar Backscatter Cross Section (σ^o) in Linear Units, (b) Ratio of the L-Band to X-Band Cross Section, (c) Relative Fluorescence F_r.

18.9°C between group "A" and group "B".

One could argue that the L-band backscatter (24 cm waves) might be more sensitive to the 1.5 m/s wind speed increase than the X-band backscatter (4 cm waves). However, this is unlikely since 4 cm waves respond to wind speed changes more rapidly than 24 cm waves. A more likely explanation is that the L-band backscatter is more sensitive to the wind direction change than the X-band backscatter. That is, the horizontally polarized Bragg scattering angular wind dependence is more sensitive to 24 cm waves than 4 cm waves. We expect the largest damping when the wind is blowing along the radar look direction for X-band (4 cm).

The largest values of relative fluorescence ($F_r \approx 7$) near 10:47 and 11:10 are approximately co-located with the minimum values in the cross section for both L-band (24 cm waves) and X-band (4 cm waves). However, some of the locations of the individual slicks do not exactly coincide when the cross section decreases. We did not investigate these location discrepancies further in the present work.

The slick characterization as a function of changing wind speed and/or direction is of interest. A considerable amount of radar imagery of surface slicks has been acquired in recent years. However, these synthetic aperture radar (SAR) images are instantaneous two-dimensional snapshot of the slicks, an example is given in Figure 6. That is, changes in cross section as a function of wind speed or direction are difficult to determine using SAR imagery. Ship-board X-band radar modulations have been reported similar to aircraft X-band SAR measurements when internal waves travel near the range direction of the radars; see, [Shuchman et al., 1988]. However, for other directions smaller image modulations were observed. Indeed, the lack of bright/dark type radar signatures in the present measurements could possibly be due to the orientation of the slicks relative to the radar look direction or alternately, slicks not associated with internal waves. We expect the maximum bright/dark signature when the slick groups are traveling in the same direction as the radar look direction. The cross sectional modulation due to straining of

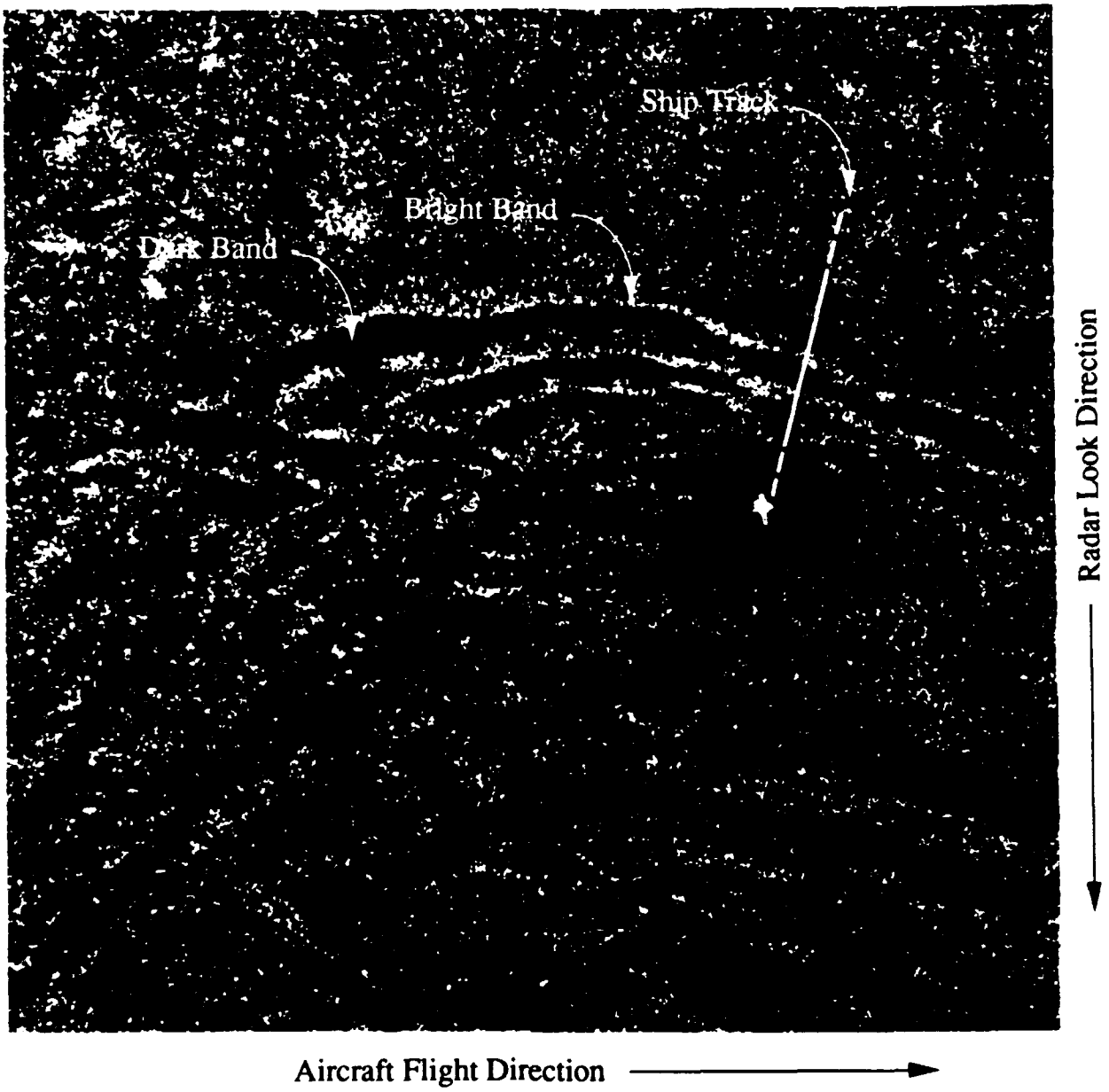

Figure 6. Synthetic Aperture Radar Image of Internal Wave Slicks in the Georgia Straits. This L-Band Radar Image Shows Long Bright and Dark Bands Induced by a Group of Internal Waves Traveling Toward the Top of the Image. The Bright Return Near the Rear of the Wave Group is a Ship.

the short waves at L-band is in reasonable agreement with the Bragg scattering theory. However, theory predicts that the X-band modulation is typically a factor of ~ 25 smaller, see equations (8) and (9). Observed radar image modulations show similar modulations at both L-band and X-band; see, e. g., Lyzenga and Bennett [1988].

The dissipation of wind driven short waves is significantly smaller for the surfactant free sea than within a slick. The surface, instead of being free, is to a first approximation represented by an inextensible (incompressible) microlayer within the slick. This is equivalent to the horizontal velocity of the particles vanishing at the interface between the microlayer and the sea water sub-layer with the vertical gradient of the velocity directly related to the losses due to viscosity at the interface. The wind input to a surfactant free sea must be sufficient to overcome the wind speed threshold which dependents on bulk viscosity of the sea. This threshold is about 1 m/s which means these short waves are essentially always present on the open (clean) ocean. The exponential decay time due to the viscosity, τ, of the short gravity waves based on a surfactant free surface (constant surface tension) is,

$$\tau \approx \lambda_b^2/8\pi^2\nu \qquad \text{(clean surface)} \tag{10}$$

where the spectral density of the short waves decreases as $\exp(-2t/\tau)$, ν is the kinematic viscosity for sea water, $\nu = 1.78 \times 10^{-2}$ cm^2 s^{-1} then $\tau \approx 0.712\ \lambda_B^2$ where the Bragg wavelength λ_b is given in centimeters. We obtain for the 4 cm and 24 cm waves, $\tau_{f24} \approx$ 400 s, $\tau_{f4} \approx$ 10 s which indicates that the shorter (4 cm) gravity waves are more rapidly damped (shorter decay time) than the 24 cm waves. However, these waves are continuously generated by the wind input. Therefore both the 4 and 24 cm waves are always present even for light winds.

The viscous damping within slicks is much larger. We consider for the moment that the short waves as generated in adjacent surfactant free regions next to the slicks and

propagated into the slick region where they are rapidly attenuated resulting in the cross section decreases as shown in Figures (4), (5) and (6). The exponential decay time, τ_f, for the short waves within a slick where large concentrations of organic material are present is approximated by an inextensible microlayer as given by Lamb [1932],

$$\tau_f \approx (8/\nu\omega_b k_b^2)^{1/2} \qquad \text{(inextensible microlayer)} \tag{11}$$

The decay time for short gravity waves are then given by, $\tau_f \approx 0.375\ \lambda_b^{5/4}$ based on deep water dispersion where λ_b is given in centimeters. The shorter wavelengths are damped more strongly than the longer wavelengths, $(\lambda_{bL}/\lambda_{bX})^{5/4} = 9.86$. However, the wind input must also be considered before the radar extracted damping can be compared with equation (11).

Applying equation (11) to the 24 cm and 4 cm waves, we obtain $\tau_{f24} \approx 20$ s, $\tau_{f4} \approx 2$ s. The viscous decay time for both the free surface and the inextensible microlayer as a function of Bragg wavelength is given in Figure 7. We have assumed for the moment that no short waves are generated within the slick. Therefore, the distance the short waves propagate into an inextensible microlayer depends on the group velocity of the short gravity waves, about 6 m for 24 cm waves and about 0.2 m for 4 cm waves. This idealized model is based on a slick which changes abruptly from a surfactant free region to an inextensible microlayer with wave reflection at the boundary neglected. However, the wind input inside slicks is required before a realistic representation of the waves inside the slick bands can be modeled. Intuitively, a slick band should approach an inextensible microlayer only near its' center with a transition to a relatively surfactant free surface with distance away from the center. The microlayer is essentially elastic in this transition region. A realistic representation of the damping must also take into account the concentration. We investigate the wind input and the wave damping in terms of the ERIM ocean model below.

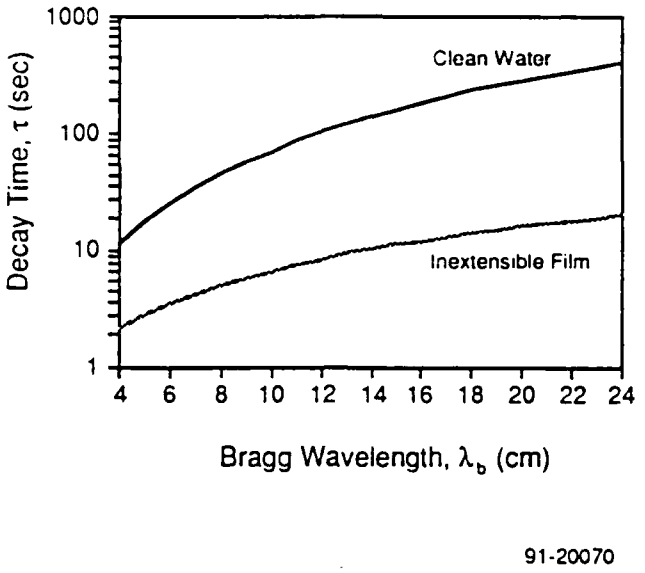

Figure 7. The Exponential Decay Time for Both the Free Surface and the Inextensible Microlayer as a Function of Bragg Wavelength Between 4 cm and 24 cm.

3.4 EOM MODEL

The ERIM Ocean Model is an integrated hydrodynamic and electromagnetic model resulting from the short ocean wave generation and dissipation within the marine microlayer [Tanis et al., 1989]. The generation and dissipation include both wave damping and straining of the short waves. We use this model to investigate the wave damping since wave straining has already been considered.

The damping of the short waves has been formulated in terms of the action density equation including wind forcing and viscous damping. The RCS is calculated at the wavelength corresponding to the Bragg resonance. This modeled cross section given in terms of the natural surfactant concentration, or more precisely the film pressure. The one-dimensional film pressure π is defined as the force per unit length exerted by the film as it spreads horizontally across the ocean surface. The model input range of film pressure is 0.01 - 32 dynes/cm. The film pressure for a clean (surfactant free) ocean surface corresponds to approximately *0.01 dynes/cm and the concentration of the* surfactant near the center of the slick band is thought to be on the order of 16 - 32 dynes/cm. The variation of RCS as a function of operating frequency (L-, C-, and X-band) and film pressure are shown in Figure 8. The polarization and incidence angle Θ were selected to correspond to SLIX '89, namely vertical transmit and vertical receive and $\Theta = 25°$. The resulting plots are not very sensitive to the polarization or the incidence angle. The radar operating wavelength includes the dual wavelength configuration used during SLIX '89 (24 cm and 4 cm ocean wavelengths) and a C-band (5.3 GHz), an intermediate ocean wavelength, 6 cm.

The EOM model results show little change in cross section at L-band (24 cm), significant changes at C-band (6 cm) and substantial change at X-band (4 cm). The cross section shows little change with radar wavelength when $\pi = 0.01$ or 1.0 dyne/cm. The cross section was essentially constant with radar wavelength except for a decrease of

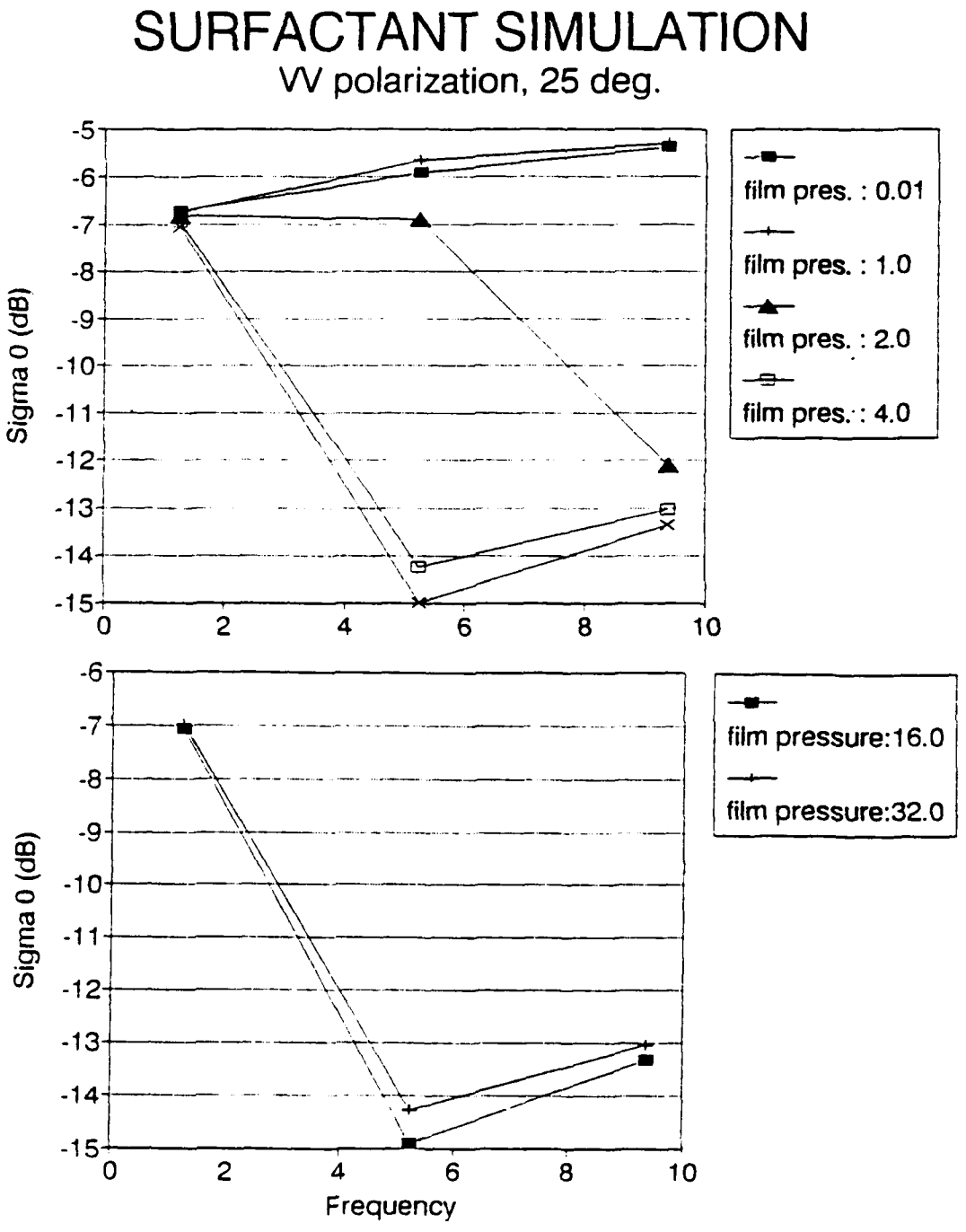

Figure 8. EOM Radar Cross Section Variation as a Function of Film Pressure π for Vertical Transmit and Receive Polarization at an Incidence Angle of 25°.

about 6 dB at X-band when π = 2.0 dynes/cm. The cross section shows significant attenuation at C-band and X-band for larger film pressures, $\pi \geq 4.0$ dynes/cm with the largest decrease at C-band rather than at the short radar wavelength X-band. We believe this larger damping at C-band than L-band or X-band is due to ocean wave coupling between the traverse and longitudinal wave; see, e. g. Alpers and Huhnerfuss [1989].

The dampening of the short waves is greater at 4 cm compared to 24 cm as measured across the slicks and as calculated by the EOM model. However, the model shows a damping ratio of about 7 - 8 dB whereas the measurements give a larger damping ratio about 12 dB, a factor of 16. Therefore the EOM model underestimates the damping at 4 cm compared to 24 cm by about 4 dB. We suggest that if more comprehensive measurements are taken, the validity of EOM may be determined which might include a cross section dependence on the relative angle between the radar look direction and the wind and internal wave directions. A validated EOM model could be used to extract the film pressure from the comparison of the model and measurement. The film pressure is a measure of the concentration of the surfactant material.

4.0. RADIOMETRIC MODEL

The radiometric temperature T_B for a near surface down-looking radiometer over a rough half space (wind sea) based on thermodynamic equilibrium is related to the sea surface temperature T_S (in °K) by,

$$T_B = e(S, U, T_S) T_S \tag{12}$$

where S is the salinity of the ocean, U is the wind speed at 20 m, e is the emissivity of the rough ocean, and $T_S(°C) = T_S(°K) - 273.16$. The emissivity for a smooth sea at normal incidence is given by,

$$e_s = 1 - \left| \frac{1-\sqrt{\epsilon}}{1+\sqrt{\epsilon}} \right|^2 \tag{13}$$

where ϵ is the complex dielectric constant of sea water.

The dielectric constant ϵ of sea water is dependent on the microwave frequency ω in rad/sec., ionic conductivity σ in mhos/m, relaxation constant τ in sec., and static dielectric constant ϵ_s [Debye, 1929] as given by,

$$\epsilon = \epsilon_\infty + \frac{\epsilon_S - \epsilon_\infty}{1 + (j\omega\tau)^{1-\alpha}} - j\frac{\sigma}{\omega\epsilon_0} \tag{14}$$

where $\epsilon_0 = 8.854 \times 10^{-12}$ is the permittivity of free space in farads/m, ϵ_∞ is the

permittivity at a high frequency, $\omega = 2\pi f$ is the radian frequency with f in Hz, α is an empirical constant and σ, τ, and ϵ are all functions of S and T_S. Empirical values of σ, τ, and ϵ as a function of S and T_S were given by Klein and Swift [1977] for the microwave frequencies 1.43 and 2.65 GHz. We use these empirical values to investigate a suitable radiometric frequency for which the emissivity dependence on salinity is negligible, see section 3.1. The selection of this frequency means that equation (12) can be simplified with T_B depending on only U and T_S,

$$T_B = e(U, T_S) T_S . \tag{15}$$

We now, in principle, can extract the wind speed U and surface temperate T_S using equation (15) and,

$$U = f^{-1}(\sigma_0) \tag{16}$$

where σ_o is the scatterometer backscattering cross section and f^{-1} is the inverse of the function f given by,

$$\sigma_0 = f(U) = aU^b \tag{17}$$

where a and b are empirical constants dependent on the scatterometer frequency and the wind direction. The extracted winds at 20 m are accurate to about $\pm$ 1 m/s based on aircraft circle flights, upwind, crosswind and downwind; see, e. g., Donelan and Pierson [1987]. If the effect of boundary layer stability is removed, increased accuracy is

expected.

The emissivity dependence on U and T_S, given in equation (15), has been modeled quantitatively by Wilheit [1979]. This numerical model originally developed by Stogryn [1967] has been simplified by Wilheit based on an isotropic normal distribution for the ocean wave slopes. Wilheit obtained good agreement between the model and radiometer measurements based on this simplification with the variance of the slope increasing linearly with the radiometric frequency. Furthermore, for high wind speeds, he also included the effect of foam on the radiometric temperature. He treated foam as partially obscuring the surface independent of polarization. We use this model in the present work. Equation (15) and this model are used to estimate the emissivity dependence on U and T_S.

4.1. SEA SURFACE TEMPERATURE RESULTS

The optimum radiometric frequency is selected such that the emissivity dependence on salinity is negligible and also such that the atmospheric effects due to water vapor and clouds are minimized. This results in the lowest frequency consistent with negligible dependence on salinity. Blume, et al. [1978] used radiometers operating at 1.43 and 2.65 GHz to measure salinity with aircraft flights over an estuary. Since both of these frequencies are sensitive to salinity, an optimum frequency must be larger than 2.65 GHz. We use equations (13) and (14) and Klein and Swift's results in the range $3 < f < 10$ GHz to investigate the minimum frequency which results in an error in radiometric temperature of less than 0.04°C per ppt in salinity. The salinity of surface water remains relatively constant for long periods of time (near 34.6 ppt) with a geographic latitude variation of about 1 ppt provided isolated areas are excluded. These areas include coastal regions, especially estuaries and melting ice in polar regions [Williams, 1962].

The results of our investigation are shown in Figure 9 (a) with the emissivity as a function of T_S with an optimum frequency of 6 GHz; while, Figure 9 (b) illustrates the same variation at 2.65 GHz for comparison. The range of salinity was varied from 20 ppt to 40 ppt in intervals of 2 ppt. Each ppt interval change in Figure 9 (a) corresponds to $\lesssim$ 0.00013 change in emissivity or equivalently $\lesssim$ 0.038 °C/ppt. Each ppt interval in Figure 9 (b) corresponds to $\lesssim$ 0.0007 or $\lesssim$ 0.22 °C/ppt. These results are based on $T_S \leq 20$ °C. Therefore the optimum radiometric frequency is near 6 GHz as given in Table 4 (a). Indeed, a typical salinity change of 1 ppt with latitude causes a change in T_S of 0.038 °C at C-band (6 Ghz) and 0.22 °C at S-band (2.65 GHz) for normal incidence.

We now consider the emissivity dependence on only U and T_S using equation (15) and Wilheit's model. The variation of the emissivity with incidence angle for three wind speeds, U = 6, 10 and 20 m/s are given in Figure 10 (a). Wind speeds less than 6 m/s have negligible foam cover. The upper three curves correspond to vertical polarization and the lower three curves to horizontal polarization. The vertically polarized curves tend to intersect at an incidence angle Θ between 50° and 60°. Therefore these incidence angles correspond to a minimum dependence on wind speed which is the same result as previously reported by Stogryn [1967]. The percent of effective foam cover for wind speeds from 8 to 20 m/s based on the model are given in Table 3. Figure 10 (b) shows the same results as Figure 10 (a) except the differential emissivity is displayed on the vertical axis. This normalized differential emissivity $\delta e/e_s$ in percent is defined as,

$$\frac{\delta e(\theta)}{e_S(\theta)} = 100 \frac{(e_S(\theta) - e(\theta))}{e_S(\theta)} \quad \% \tag{18}$$

where $e_s(\Theta)$ is here the emissivity of the smooth sea as a function of incidence angle and

TABLE 3.

Wind Speed and Associated Percent Effective
Foam Cover Based on Wilheit's Model

U(m/s)	FOAM(%)
6	0
8	.33
10	.99
12	1.65
14	2.31
16	2.97
18	3.63
20	4.31

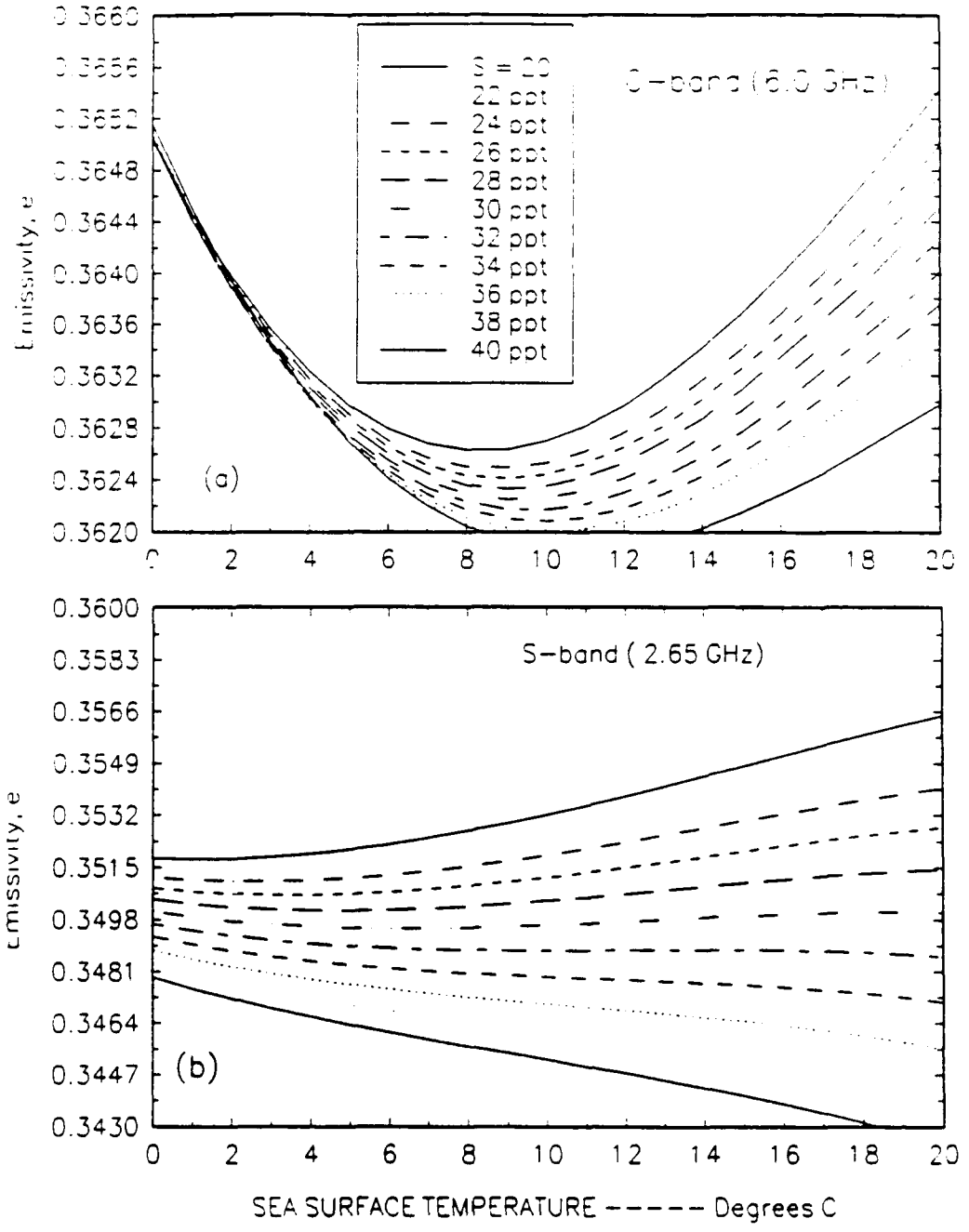

Figure 9. Emissivity Variation With Sea Surface Temperature Based on a Smooth Sea Parameterized in Salinity at Normal Incidence Using: (a) Radiometric Frequency of 6 GHz (C-Band), and (b) Radiometric Frequency of 2.65 GHz (S-Band).

TABLE 4.

Radiometric Brightness Temperature Sensitivity to:
(a) Salinity at Normal Incidence, (b) Wind Speed, S = 34 ppt And $\Theta = 60°$

(a)

	OPERATING FREQUENCY	
	C-BAND (6 GHz)	S-BAND (2.65 GHz)
$\Delta T_B/\Delta S$	0.038°C/ppt	0.22°C/ppt

(b)

C-BAND (6 GHz)	POLARIZATION	
	VERTICAL	HORIZONTAL
$\Delta T_B/\Delta U$	$\lesssim$ 0.12°C/m/s	$\lesssim$ 2.0°C/m/s

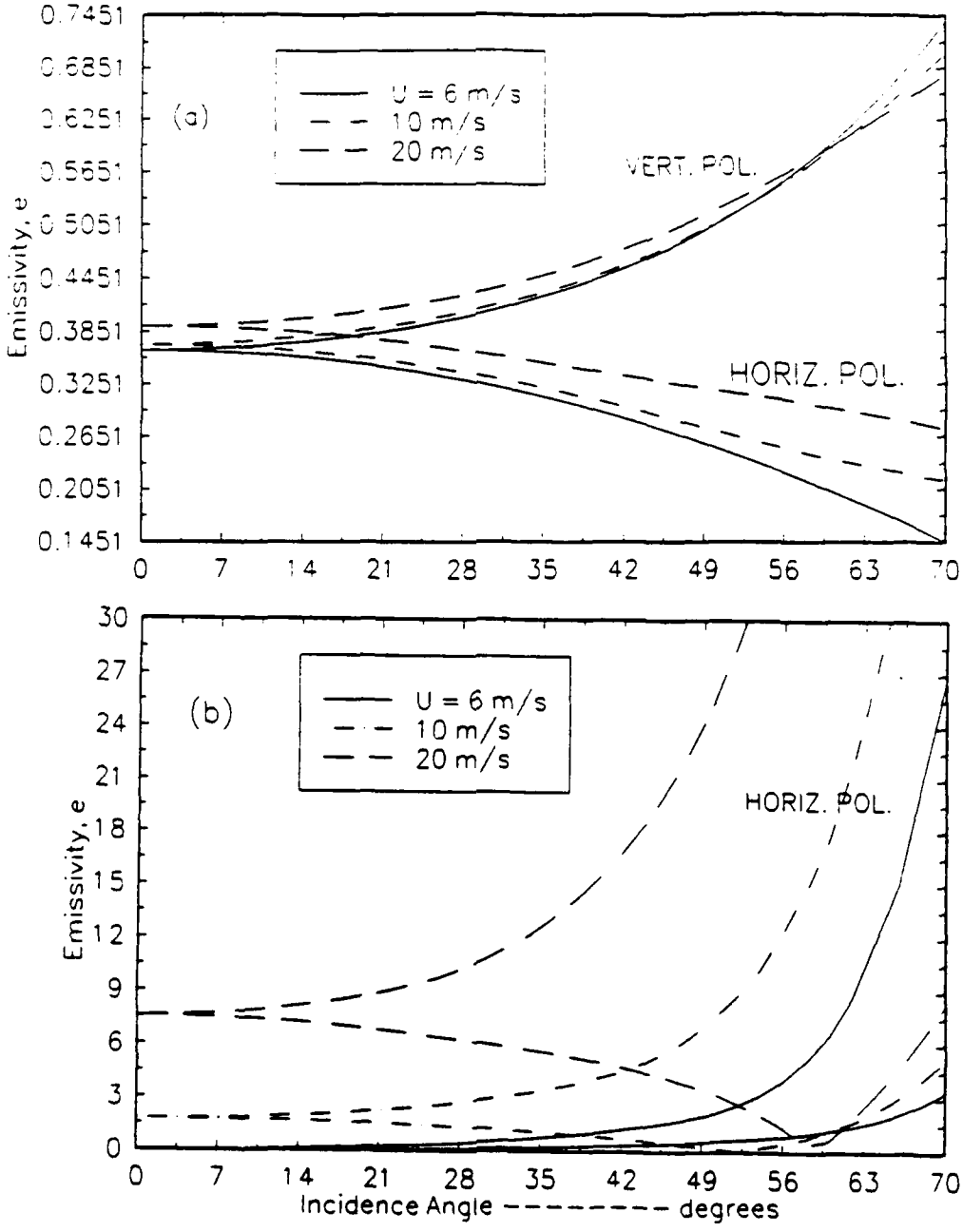

Figure 10. Emissivity Variation With Incidence Angle Parameterized in Surface Wind Speed, 6 m/s, 10 m/s and 20 m/s. The Salinity is 34 ppt and the Sea Surface Temperature is 18°C. The Upper Three Curves Correspond to Vertical Polarization and the Lower Three Curves Correspond to Horizontal Polarization; (a) Emissivity, and (b) Differential Emissivity.

$e_{sH}(\Theta)$ and $e_{sV}(\Theta)$ are the corresponding vertical and horizontal polarizations of $e_s(\Theta)$ given by,

$$e_{sH}(\theta) = 1 - \left| \frac{\cos\theta - \sqrt{\epsilon - \sin^2\theta}}{\cos\theta + \sqrt{\epsilon - \sin^2\theta}} \right|^2 \tag{19}$$

$$e_{sV}(\theta) = 1 - \left| \frac{\epsilon\cos\theta - \sqrt{\epsilon - \sin^2\theta}}{\epsilon\cos\theta + \sqrt{\epsilon - \sin^2\theta}} \right|^2 \tag{20}$$

The three lower curves correspond to vertical polarization and the three upper curves correspond to horizontal polarization. The differential emissivity for the vertical polarization consistently shows a lower percent variation as a function of incidence angle and wind speed.

We next consider the emissivity dependence on sea surface temperature for a range of wind speeds, U = 6 - 20 m/s at $\Theta = 60°$. Figure 11 (a) shows the emissivity dependence on U and T_S for horizontal polarization whereas Figure 11 (b) shows this same dependence for vertical polarization. The primary result here is that the vertical polarized T_B^V is only weakly dependent on wind speed when 6 m/s $\leq$ U $\leq$ 10 m/s whereas at higher wind speeds the change in emissivity is $\Delta e/\Delta U \lesssim 0.00042$/m/s or in terms of T_B^V is $\Delta T_B^V/\Delta U \lesssim 0.12°C$/m/s. In contrast, the change in emissivity for horizontal polarization is $\Delta e/\Delta U \lesssim 0.007$/m/s or $\Delta T_B^H/\Delta U \lesssim 2.0°C$/m/s when U > 6 m/s. These T_B sensitivities to wind speed are summarized in Table 4 (b). The maximum error is $\pm$ 0.12°C and $\pm$ 2.0°C for T_B^V and T_B^H respectively based on the scatterometer wind accuracy of $\pm$ 1 m/s. That is, this analysis assumes no errors in the model and the measurement of the T_B^V and T_B^H. This result suggests that a scatterometer can be used

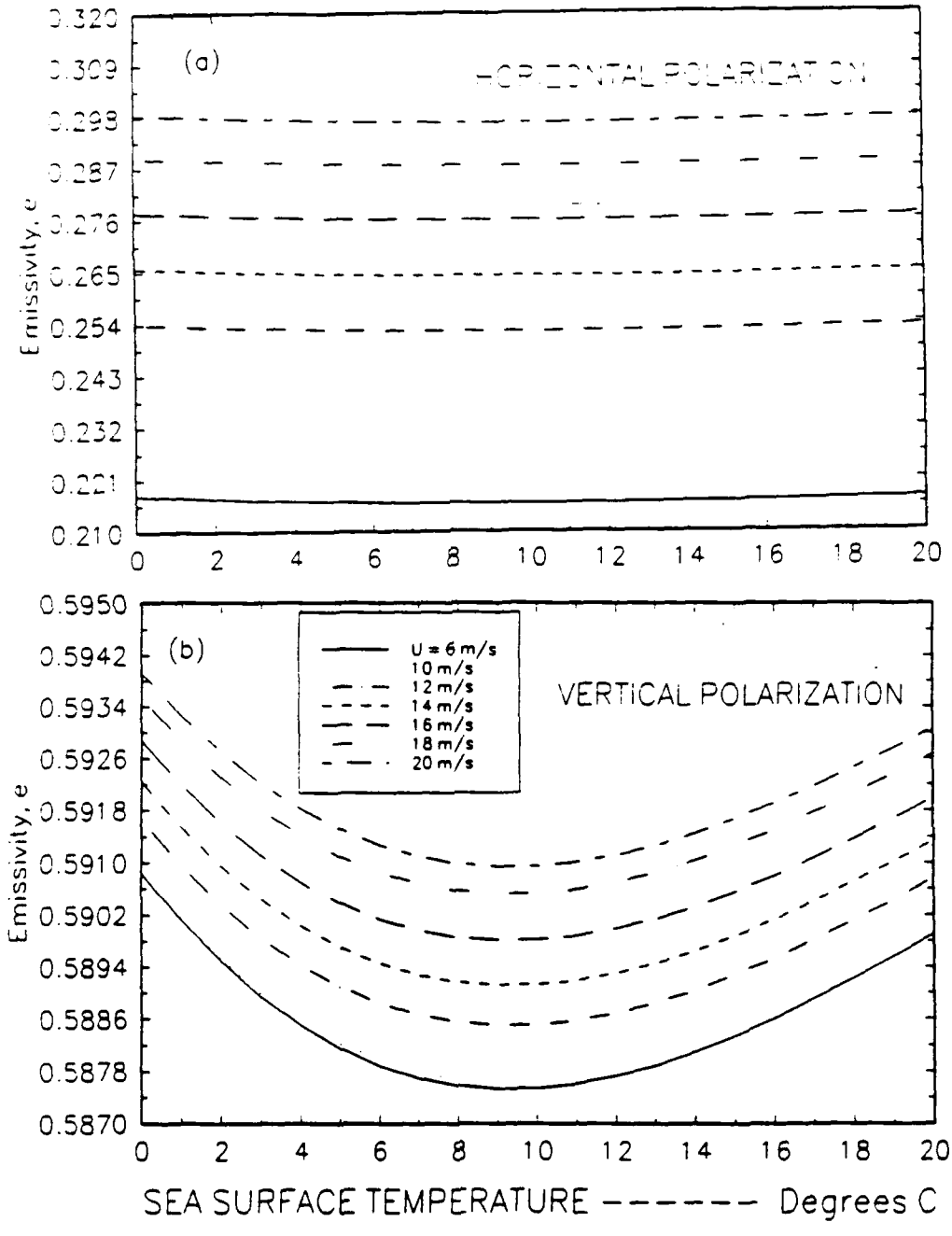

Figure 11. Emissivity Variation with Sea Surface Temperature Parameterized in Surface Wind Speed, 6 - 20 m/s, Incidence Angle = 60° and Salinity = 34 ppt; (a) Horizontal Polarization, and (b) Vertical Polarization.

to correct a radiometer with a vertical polarized pencil antenna beam operating near 6 GHz with an incidence angle near 60°.

5.0 PROPOSED FURTHER ANALYSIS AND FUTURE EXPERIMENTS

We propose analysis of the radiometer measurements on October 16 during SLIX '89 when a temperature front was intersected by the research vessel, see section 5.1. Furthermore, we propose two new experimental programs:

(1) Simultaneous scatterometer, radiometer and SCUMS measurements from a ship platform across natural slicks at times when radar images of the slick are available. This experiment is similar to SLIX '89 except we require radar imagery in addition to the other measurements.

(2) Simultaneous scatterometer and radiometer measurements from an ocean tower acquired over a sufficiently long period of time that a wide range of ocean/atmospheric conditions are observed including ocean temperature fronts and wind speeds ranging over, say, 0 to 20 m/s.

5.1 RECOMMENDED ADDITIONAL ANALYSIS OF SLIX '89

The research vessel Wecoma, during SLIX '89, traversed a temperature front where the temperature change was about 1° C to 2° C on October 16. We suggest the radiometric temperatures be analyzed for the passive microwave sensors on both sides of this temperature front.

5.2 PROPOSED FUTURE EXPERIMENTS

Two experiments are proposed as summarized in section 5.0.
The first experiment would include simultaneous scatterometer, radiometer, and SCUMS

measurements across natural occurring slicks when auxiliary quantitative information is available on both the surface wind speed and direction, and the slick spacing and orientation. Second, we propose an experiment to establish the feasibility of extracting sea surface temperature from simultaneous active/passive measurements.

The slick experiment would require an imaging radar be flown over the experiment area to measure the slick spacing and orientation in addition to the microwave and SCUMS measurements. This imagery could also be useful in establishing the mechanism responsible for the slicks as well as any azimuthal dependence of the slick orientation relative to the scatterometer look direction. Furthermore, the radar images may be useful in spatially locating any surface wind fronts in the area. The anemometer measured winds would be continuously acquired aboard the research vessel.

The proposed experiment to extract the sea surface temperature would use a surface-based radiometer operating at 6 GHz with data acquired on both horizontal and vertical polarized antennas using a pencil beam, say $\Delta\Theta \leq 2°$, selected at an incidence angle near 55° as suggested by Figure 10 (b). These measurements would be acquired in conjunction with scatterometer and wind anemometer measurements in an area where high winds and ocean temperature fronts frequently occur allowing the validation of the model and the measuring technique.

6.0 SUMMARY

The limited measurements reported here show that the peaks in fluorescence, related to the peak concentration of Chlorophyll A, are co-located with the damping of the short gravity waves at both 4 cm and 24 cm wavelengths. The maximum damping ratio between the 24 cm and 4 cm waves is at least 16 for a wind direction of about 30° with respect to the radar look direction and wind speeds, 3-4 m/s.

Imaging-radar slick signatures displaying narrow bright bands on the leading edge of a series of wider dark slick bands have been interpreted as due to short wave straining by internal waves. We assert that the wide dark bands following these bright bands, when observed, are primarily due to wave damping. That is, these dark bands are related to increased concentration of the marine surface microlayer material. Therefore, the radar roughness of slicks on some occasions may be caused by both short wave damping and wave straining of the short gravity waves.

We propose two future experiments: (1) simultaneous shipboard microwave sensor and SCUMS measurements across naturally occurring slicks similar to SLIX '89 except that radar imagery would also be acquired during the experiment, and (2) simultaneous active/passive measurements from an ocean tower using a radiometer with both vertical and horizontal polarization, pencil beam antenna patterns at an incident angle of 55° and an operating frequency of 6 GHz. In addition to these radiometer measurements, simultaneous scatterometer and anemometer measurements would also be acquired on the tower.

7.0 BIBLIOGRAPHY

Alpers, W. R., Theory of Radar Imaging of Internal Waves, Nature 314 (6008), 245-247, 1985.

Alpers, W., and H. Huhnerfuss, The Dampening of Surface Films: A New Look at an Old Problem, J. Geophy. Res. 94(C5), 6251-6265, 1989.

Apel, J. R. and F. I. Gonzalez, Non-linear Features of internal waves off Baja California as Observed from the SEASAT Imaging Radar, J. Geophys. Res., 88, 4459-4466, 1983.

Blume, H. C., B. M. Kendall, and J. C. Fedors, Measurement of Ocean Temperature and Salinity Via Microwave Radiometry. Boundary Layer Met. 13, 295-308, 1978.

Carlson, D. J., Surface Microlayer Phenolic Enrichment Indicates Sea Surface Slick, Nature, 296, 426-429, 1982.

Carlson, D. J., Viscosity of Sea-Surface Slicks, Nature, 329, 823-825, 1987.

Carlson, D. J., J. L. Cantey and J. J. Cullen, Description of and Results From a new Surface Microlayer Sampling Device, Deep Sea Res., 35(7), 1205-1213, 1988.

Debye, P., Polar Molecules (New York, Dover reprint; original Reinhold), 1929.

Donelan, M. A., and W. J. Pierson, Radar Scattering and Equilibrium Ranges in Wind-Generated Waves With Application to Scatterometry. J. Geophys. Res. 92(C5), 4971-5029, see section 7, 1987.

Ewing, G., Slicks, Surface and Internal Waves, J. Mar. Res., 9(3), 161-187, 1950.

Gasparovic, R. F., J. R. Apel and E. S. Kasischke, An Overview of the SAR Internal Wave Signature Experiment, J. Geophys. Res., 93(C10), 12,304-12,316, 1988.

Hollinger, J. P., Passive Microwave Measurements of Sea Surface Roughness. IEEE Trans. Geosci. Elect. GE-9(3), 165-169, 1971.

BIBLIOGRAPHY (CONTINUED)

Hühnerfuss, H., and W. Alpers, Molecular Aspects of the System Water/Monomolecular Surface Film and the Occurrence of a New Anomalous Dispersion Regime at 1.43 GHz, J. Phys. Chem., 87, 5251-5258, 1983.

Klein, L. A., and C. T. Swift, An Improved Model for the Dielectric Constant of sea Water at Microwave Frequencies. IEEE Trans. Ant. Prop. AP-25(1), 104-111, 1977.

LaFond, E. C., Internal Waves, in the Sea, vol 1, M. N. Hill (Ed.), Interscience Publishers, New York, 1962.

Levich, V. G., Physicochemical Hydrodynamics, Prentice Hall, Inc., Englewood Cliffs, N. J., 1962.

Lamb, H., Hydrodynamics, Dover Publications Inc., New York, pp 623-632, 1932.

Lyzenga, D. R., and J. R. Bennett, Full Spectrum Modeling of Synthetic Aperture Radar Internal Wave Signatures, J. Geophys. Res. 93, 12,345-12,354, 1988

Mitsuyasu, H., and T. Honda, The Effects of Surfactant on Certain Air-Sea Interaction Phenomena, in Wave Dynamics and Radio Probing of the Ocean Surface (Ed., O. M. Phillips and K. Hasselmann) Plenum Press, New York, 1986.

Plant, W. J., A Relationship Between Wind Stress and Wave Slope, J. Geophys. Res. 87(C3), 1961-1967, 1982.

Rufenach, C. L., and C. Smith, Observation of Internal Waves in LANDSAT and SEASAT Satellite Imagery, Int. J. Remote Sensing, 6, 1201-1207, 1985.

Shuchman, R. A., D. R. Lyzenga, B. M. Lake, B. A. Hughes, R. F. Gasparovic, and E. S. Kasischke, Comparison of Joint Canada-U.S. Ocean Wave Investigation Project Synthetic Aperture Radar Data With Internal Wave Observations and Modeling Results, J. Geophys. Res. 93, 12,283-12,291, 1988.

BIBLIOGRAPHY (CONCLUDED)

Stogryn, A., The Apparent Temperature of the Sea at Microwave Frequencies, IEEE Trans. Ant. Prop. AP-15(2), 278-286, 1967.

Swift, C. T., Microwave Radiometer Measurements of the Cape Cod Canal. Radio Sci. 9, 641-654, 1974.

Tanis, F. J., J. R. Bennett and D. R. Lyzenga, Physics of EOM, ERIM Technical Report No. 28, Ann Arbor, Michigan, 1989.

Valenzuela, G. R., Theories for the Interaction of Electromagnetic and Oceanic Waves - A Review, Boundary Layer Meteorol. 13, 61-85, 1978.

Wilheit, T., A Model for the Microwave Emissivity of the Ocean's Surface as a Function of Wind Speed. IEEE Trans. Geosci. Elect. GE-17(4), 244-249, 1979.

Wilheit, T., A. T. C. Chang, and A. S. Milman, Atmospheric Corrections to Passive Microwave Observations of the Ocean. Boundary Layer Met. 18, 65-77, 1980.

Williams, J, Oceanography: An Introduction to Marine Science, Little, Brown and Co., Boston, 1962.

APPENDIX

PUBLICATIONS RESULTING FROM THIS RESEARCH

ACTIVE AND PASSIVE MICROWAVE MEASUREMENTS OF NATURAL SURFACE SLICKS DURING SLIX'89

Robert G. Onstott
Robert A. Shuchman
Scott Gaboury
David R. Lyzenga

Environmental Research Institute of Michigan

Presented at IGARSS '90, College Park, Maryland, 20-24 May 1990

ACTIVE AND PASSIVE MICROWAVE MEASUREMENTS OF NATURAL SURFACE SLICKS DURING SLIX'90

Robert G. Onstott, Robert A. Shuchman,
Scott Gaboury, and David R. Lyzenga

Radar Science Laboratory
Advanced Concepts Division
Environmental Research Institute of Michigan
Ann Arbor, MI 48107 USA

ABSTRACT

During the October 1989 Marine Microlayer Slick Experiment (SLIX'89) which occurred off the coast of San Diego and Santa Rosa Island, L-, C-, X-band scatterometer and C- and Ka-band radiometer measurements were made from the R/V Wecoma of surface slicks associated with fronts and naturally occurring internal waves (IWs). The Wecoma operated in situ measuring devices as it traversed the IW generated slicks. The instrumentation which operated coincidently with the active and passive microwave sensors included the SCUMS catamaran with surface potential, laser slope, ADCP, thermistor fin, and second harmonic surface probes.

Microwave measurement were made both in the slick and surfactant free areas for comparison purposes. A range of incident angles were collected to demonstrate Bragg resonant effects due to the slick material. Initial examination shows significant differences in both radar backscatter (σ^o) and microwave brightness temperature due to the presence of slicks.

INTRODUCTION

The ability to discriminate ocean surface features caused by slicks, fronts, and eddies, the microwave response, backscatter and emission, of a wind driven sea, were the focus of this investigation. Overall goals include improving the estimates of windspeed and direction and sea surface temperature when using data products acquired via satellite sensors.

MEASUREMENTS

The microwave and slick-ocean measurements (See Table 1) were designed to retrieve information from patches of ocean surface observed coincidently with each sensing system. During the measurement period winds ranged from 2 to 15 knots, with wave classes ranging from glass-like to white-capped. Slicks occurred in distinct narrow bands or were regional. Fronts with 1° temperature difference and ocean eddies were observed during transit.

Of particular interest is the relationship of slick properties to the microwave response as examined in the frequency and angular response characteristics of the backscatter depression response determined from non-slick and slick conditions. Slick-induced roughness variations were directly sensed using the scatterometers. Radiometer measurements were made to determine the resultant effect on emissivity.

Additionally, the hypothesis that backscattering is explained by Bragg scattering was tested by comparing radar frequency-angle combinations which have the same Bragg wavelength (i.e. X-20° & C-40°, C-20° & L-70°).

EXAMPLE RESULTS

In the example shown in Figure 1, the specular backscatter component was enhanced at angles near vertical under slick conditions, while at angles from 40° to 60°, enhancements to 5 dB were produced during non-slick conditions at X-band.

ACKNOWLEDGEMENTS

This work is supported by the Office of Naval Research (ONR) under contract N00014-89-C-0117. The Technical Monitor was Dr. Frank Herr.

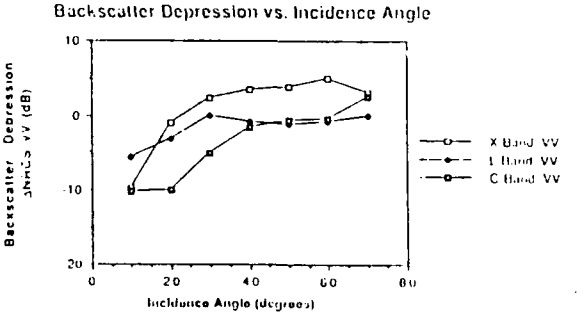

Figure 1. Backscatter Depression Versus Incidence Angle at X-, C-, and L-band and VV-Polarization During Slick and Non-Slick Conditions.

Table 1. SLIX '89 Sensor Description

Sensors	Measurements
Radars	Scattering Coefficients 1.5, 5, 10 GHz 10° to 85° Incidence
Radiometers	Brightness Temperatures Emissivities 5.6 and 35 GHz 10° to 85° Incidence
Chemical	Surface Potential Composition & Biology
Laser Wave Slope	Capillary-Gravity Waves
ADCP	Near-Surface Velocity & Turbulence
Thermistor Fin	Near-Surface Temp. Depths of 5, 10, 15 cm
Microlayer Sampler	Absorbance & Fluorescence

SHIPBOARD ACTIVE AND PASSIVE MICROWAVE MEASUREMENT OF OCEAN SURFACE SLICKS OFF THE SOUTHERN CALIFORNIA COAST

Robert Onstott and Clifford Rufenach
Environmental Research Institute of Michigan
Ann Arbor, Michigan 48107

and

David J. Carlson
College of Oceanography
Oregon State University
Corvallis, Oregon 97331

April, 1991

Accepted for publication in the Journal of Geophysical Research

ABSTRACT

Ship-based radar scatterometer measurements at L-band and X-band and microlayer Chlorophyll fluorescence measurements on the southern California continental shelf were acquired across several surface slicks during October, 1989. These measurements allowed the simultaneous extraction of both the short wave damping at Bragg wavelengths 24 cm and 4 cm and the Chlorophyll A biological concentration with sufficient spatial resolution to observe features within individual slick bands.

The measurements show: (1) the largest peaks in fluorescence, a measure of the peak Chlorophyll A concentration, are co-located with the short wave damping at 24 cm and the 4 cm wavelengths, (2) the maximum damping ratio, between the 24 cm and 4 cm waves is at least 16 for wind speeds, 3-4 m/s, and (3) the radar roughness signatures at these short Bragg gravity wavelengths suggest the slicks are caused by damping rather than straining of these waves. Additional shipboard measurements are needed to further quantify these preliminary results.

1.0 INTRODUCTION

Ship-based radar backscatter (scatterometer) and passive microwave (radiometric) measurements from the ocean surface were acquired during the October, 1989, Marine Micro-layer Slick Experiment (SLIX'89). Coincident *in situ* measurements were also taken from a catamaran, mounted with the Self Contained Underway Microlayer Sampler (SCUMS), towed from the side of the ship including a rotating drum onto which the surface microlayer material was attached [Carlson et al., 1988]. This microlayer material was collected from the rotating drum and analyzed using UV absorbance and fluorescence detectors. These ship-based measurements provided simultaneous high spatial resolution microwave and *in situ* measurements with sufficient resolution to identify coincident features inside individual slicks. The area selected for these measurements was the southern California continental shelf were slicks are frequently observed [Ewing, 1950].

Radar scatterometers measure the ocean surface roughness at Bragg wavelengths, 3 cm - 30 cm, within the radar's antenna beamwidth. Fluorescence detectors measure the concentration of the biological material, chlorophyll A; whereas, the UV absorbance detectors (280 nm) measure the concentration of chemical material. The ability of the microlayer to dampen short waves increases with the concentration of the microlayer material. This concentration varies across slicks due to the horizontal convergence of ocean currents at the surface and/or by horizontal convergence due to wind stress. That is, the surface roughness near and within slick bands vary with ocean current and wind. Slicks on the southern California and Baja continental shelf can be due to internal waves currents, small scale ocean circulation and wind stress. The internal waves typically travel along the thermocline at the same speed as the companion slick bands. These slicks are characterized by a series of slick packets; each packet separated by a distance of 15 - 20 km with an envelope of quasi-period parallel slick bands with wavelengths of about 300 km [Ewing, 1950; and Apel and Gonzalez, 1983]. The slick characteristics can be used to distinguish internal wave generated slicks from other slick generating mechanisms.

The surface roughness at short gravity wavelengths associated with quasi-periodic slicks have been observed by a number of workers using different measuring methods; see, e. g., Ewing [1950], LaFond [1962], Rufenach and Smith [1985], Alpers [1985], Shuchman et al. [1988], Lyzenga

and Bennett [1988] and Gasparovic et al. [1988]. Alternating bright and dark bands in radar images have been interpreted as horizontal current gradients produced by internal waves; see, e. g., Alpers [1985]; or equivalently, increases and decreases in radar cross-section. In contrast, radar cross-section decreases are directly related to the damping of these short waves due to increases in the concentration of the surface marine microlayer material. Surface roughness changes have usually been interpreted in terms of either damping or straining of the short waves but not both. We believe that both mechanisms may be important on some occasions.

The concentration of the surface microlayer material has been related to the bulk viscosity [Carlson, 1982; Carlson, 1987]. Microlayer viscous damping is caused by either the bulk viscosity, syrupy nature of the surface layer, or the elasticity, visco-elastic nature of this thin surface layer. The elastic properties are equivalent to an additional viscosity of the surface microlayer [Levich, 1962]. We do not attempt to distinguish between these two viscous damping mechanisms.

Detection of bands of slicks associated with internal waves by passive microwave sensors have not been reported. Passive microwave sensors have been primarily operated from spaceborne platforms with a spatial resolution $\geq$ 20 km. This resolution could explain the lack of detection since the slick packet spacing is typically 10 - 15 km. Increases in emissivity have been measured across manmade oil slicks by microwave sensors [Hollinger and Mannella, 1973] whereas one example of a large emissitivity decrease has been reported across a manmade monomolecular slick [Hühnerfuss and Alpers, 1983]. Additional shipboard multi-frequency active and passive microwave measurements in conjunction with *in situ* measurements across manmade and natural slicks are needed to better understand the radio perturbations caused by surface slicks

This study is limited to a comparison of scatterometer and radiometer measurements with *in situ* fluorescence measurements near two surface slick groups off the California coast. These measurements are interpreted in terms of straining and damping of the short gravity waves within these two slick groups.

2.0 Experimental Description

The ship-board SLIX'89 experiment was designed to traverse surface slicks off the coast of southern California near San Diego during a two week period in October 1989. The ship heading during the experiment was selected to intersect slick groups visually observed from the bridge of the ship. This experiment included a variety of *in situ* and remote sensing instruments including the microwave sensors and SCUMS catamaran *in situ* detectors.

The microwave sensors were mounted about 10 m above the sea surface toward the bow of the ship, R/V Wecoma, whereas the *in situ* instruments were towed by a catamaran attached to a boom on the port side of the ship. The wind velocity at a height of about 10 m was measured near the bow of the ship and sea surface temperature was measured at a depth of 15 cm. We operated the following microwave sensors:

(1) a dual wavelength radar scatterometer, and

(2) a dual wavelength radiometer,

both mounted on the port side with their antennas pointing perpendicular to the ship's track. The radar operating wavelengths were L-band and X-band (20 cm and 3.2 cm) while the radiometers operated at C-band and Ka-band wavelengths (5.5 cm and 0.86 cm). The radiometer outputs were carefully monitored for interference from the scatterometer. The relevant instrument parameters are given in Table 1. The radiometers were calibrated using a hot absorber and cold (near zenith sky scan) load.

The *in situ* measurements of interest were taken on board the catamaran towed about 20 m aft of the microwave sensors from the port side of the ship, SCUMS [Carlson et al., 1988]. The UV absorbance is related to the concentration of the absorbing organic molecules, whereas the chlorophyll A fluorescence is related to the concentration of the biota. The SCUMS measurements include: the fluorescence and the UV absorption measured in both the microlayer and sub-layer. The microlayer material was attached to a rotating drum then skimmed from the drum surface whereas the sub-surface material was collected at a depth of about 15 cm. The microlayer is thought to be 50-100 μm thick. The fluorescence and UV absorbance show similiar variation across the slicks implying that the

TABLE 1. SCATTEROMETER AND RADIOMETER SYSTEM PARAMETERS

	RADAR		RADIOMETER	
FREQUENCY	1.5 GHz	9.38 GHz	5.4 GHz	35 GHZ
WAVELENGTH	20 cm	3.2 cm	5.5 cm	0.86 cm
ANTENNA SPOT SIZE at $\theta = 55°$ at $\theta = 25°$ §	 3.7 m 1.5 m	 1.3 m 0.5 m	 5.3 m 2.1 m	 5.3 m 2.1 m
INTEGRATION TIME	50 sec	50 sec	50 sec	50 sec
BANDWIDTH	350 MHz	575 MHz	70 MHz	500 MHz
POLARIZATION	HH,VV or VH	HH,VV or VH	H or V	H or V
RESOLUTION	1.1 dB	2.6 dB	0.21°K	0.12°K
ABSOLUTE ACCURACY	± 1 dB	± 1 dB	± 1°K	± 1°K

* H signifies horizontal polarization and V signifies vertical polarization.

§ incidence angle used during measurements across slick groups "A" and "B" on October 16.

concentration of the surface microlayer material can be represented to first order by either detector.

A side view of the ship, catamaran and remote sensing instruments are shown in Figure 1(a) and a side view of the catamaran and associated instrumentation is shown in Figure 1(b). A photograph of the microwave antennas are given in Figure 2. Selected measurements during the SLIX experiment are given in the following section.

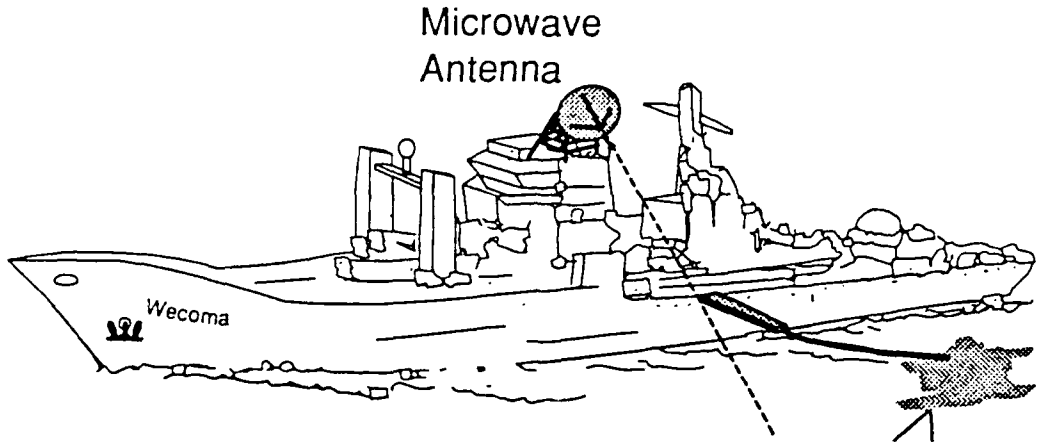

Figure 1(a). Artists Rendition of the Research Vessel Wecoma Relative to Towed Catamaran (SCUMS). The Microwave Equipment Measures Radar Cross-Section and Radiometric Brightness Temperature. The SCUMS Instrument Measures Fluorescence and UV Absorbance of the Surface Layer Organic Material.

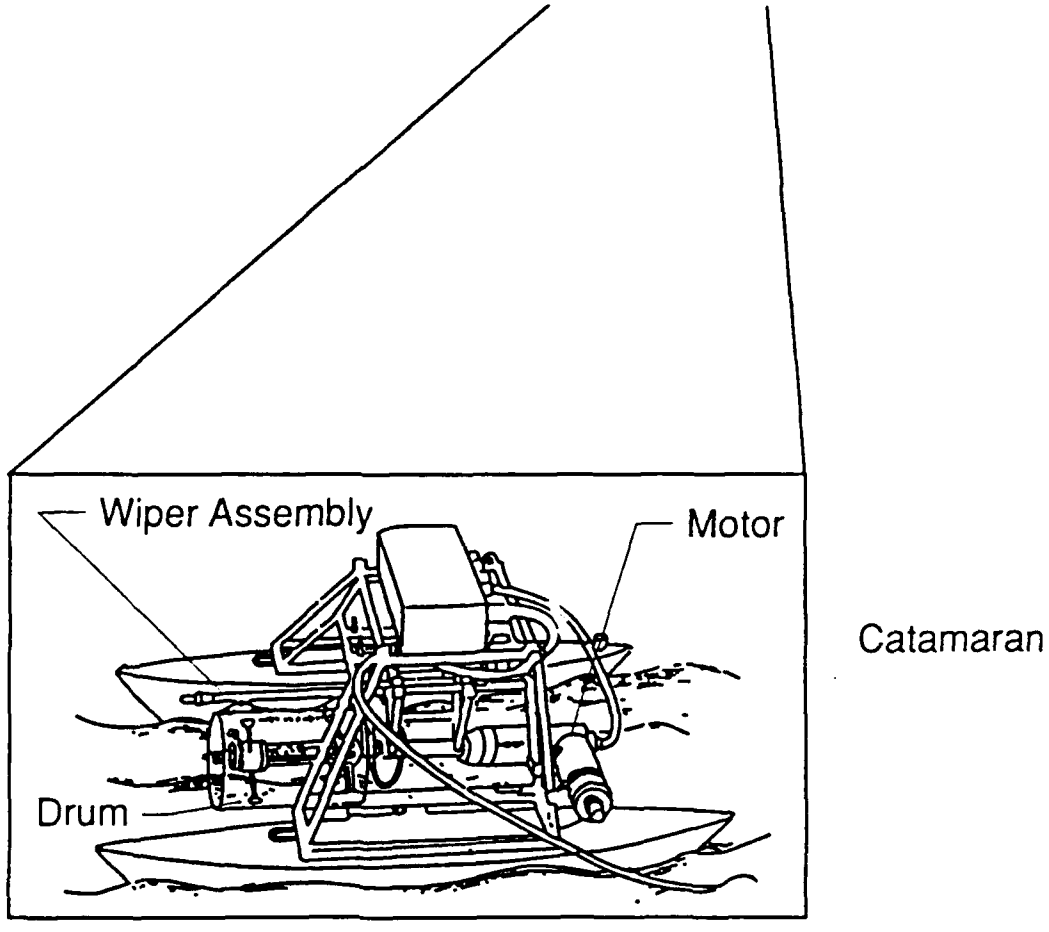

Figure 1(b). Side View of the Catamaran and Attached SCUMS Sampler. The Micro-Layer Film Attaches Itself to the Rotating Cylindrical Mirror Surfaced Drum. The Microlayer Material is Extracted From the Drum and Pumped into the Ship Where it is Analyzed.

91-20063

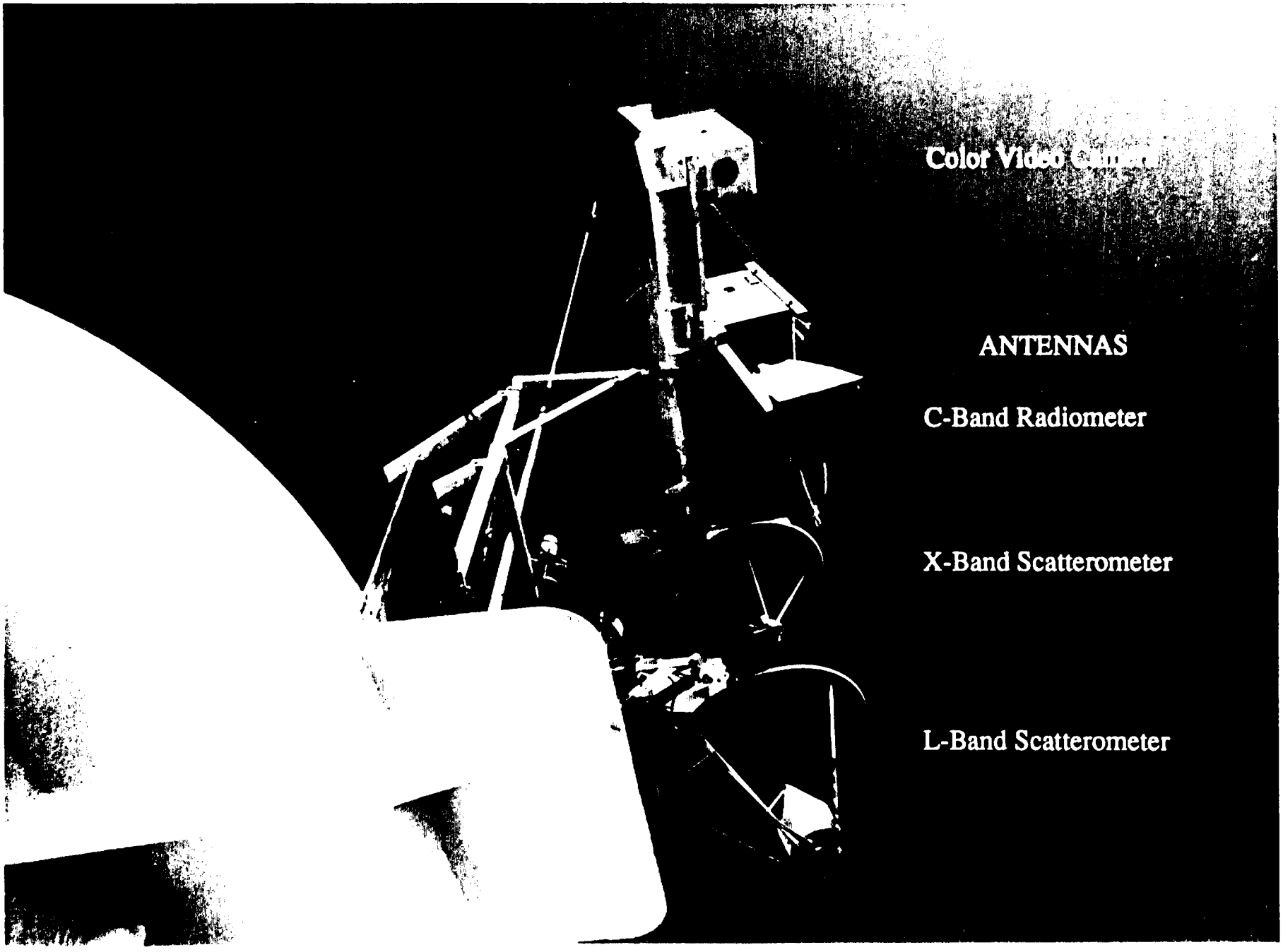

Figure 2. Photograph of the Radio Microwave Sensors: Radar Scatterometers and Passive Radiometers.

3.0 MEASUREMENTS

Two surface slick groups off the coast of San Diego during October 16 were selected for analysis. These two groups each exhibit three slick bands during a period when both the microwave and *in situ* instruments were operating. Furthermore, these two slick groups were visually observed from the ship deck as recorded in the operational log. We distinguish between groups and packets in the present work: packets are associated with internal waves; typically separated by 15 - 20 km. Groups are more closely spaced clusters of slick bands, several occurring within a packet, due to the complex nature of the bands or generating mechanisms other than internal waves. The orientation of these slick bands relative to the radar look direction is not known since radar imagery was not available and no orientation information was recorded in the log. However, the experiment objective was to traverse the slick bands. That is, the fluorescence and radar measurements show a fluctuating component along the ship track.

We have no direct measurements in the water column that these slicks were produced by internal waves or any other mechanism. However, the separation between the two groups ($\approx$ 30 min.) and a slick band spacing (3 - 5 min.), see Figure 4, suggest spatial separations; the order of a few km and hundreds of meters, respectively. The 3 - 5 min. quasi-periodic spacing are consistent with internal wave produced slick bands provided the ship speed (0.5 - 1 m/s) is much larger than that component of the slick velocity along the ship track. The spatial separation of a few km imply that the two slick groups are not internal wave associated packets. The grey areas indicated in Figure 3 give the location of the two slick groups relative to the ship track during October 16. The two slick groups occurred in the morning hours between 10:40 to 11:20 Pacific Daylight Time (PDT). There were no clouds or rain during this period.

An overview of the microwave and *in situ* measurements using stacked plots of the various parameters is given in Figure 4. The measured parameters (1 min averages) are displayed on the ordinate and the time in minutes is displayed on the abscissa in all the plots. The values of radar cross-section (σ°), fluorescence relative to the sub-layer (F_r) and radiometric brightness temperature (T_B) were selected for display. The two σ°'s at L-band and X-band are indicated in Figure 4(a). The relative slick fluorescence (F_r) is obtained by dividing the microlayer fluorescence by the sub-layer fluorescence. The inherent delay in skimming and pumping the

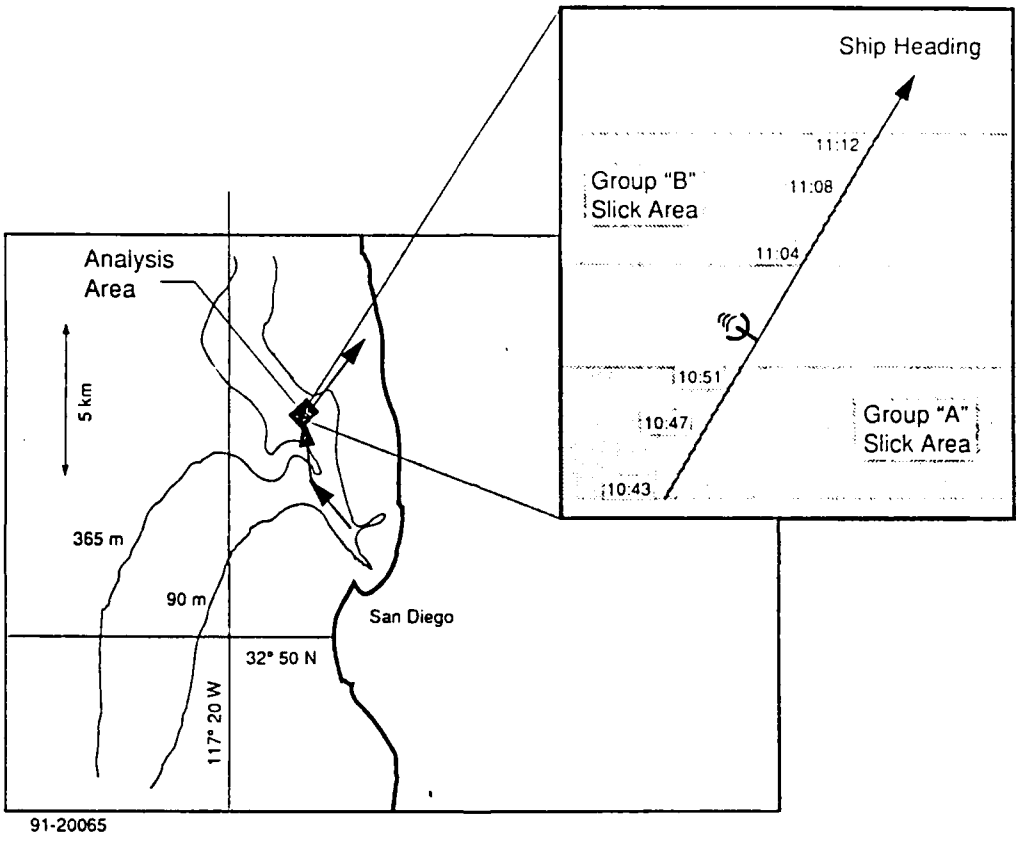

Figure 3. Plan View of Ship Track and Areas of Surface Slick Group on the R/V Wecoma on October 16, 1989. The Ocean Depth is Indicated by the Contours 90 m and 365 m.

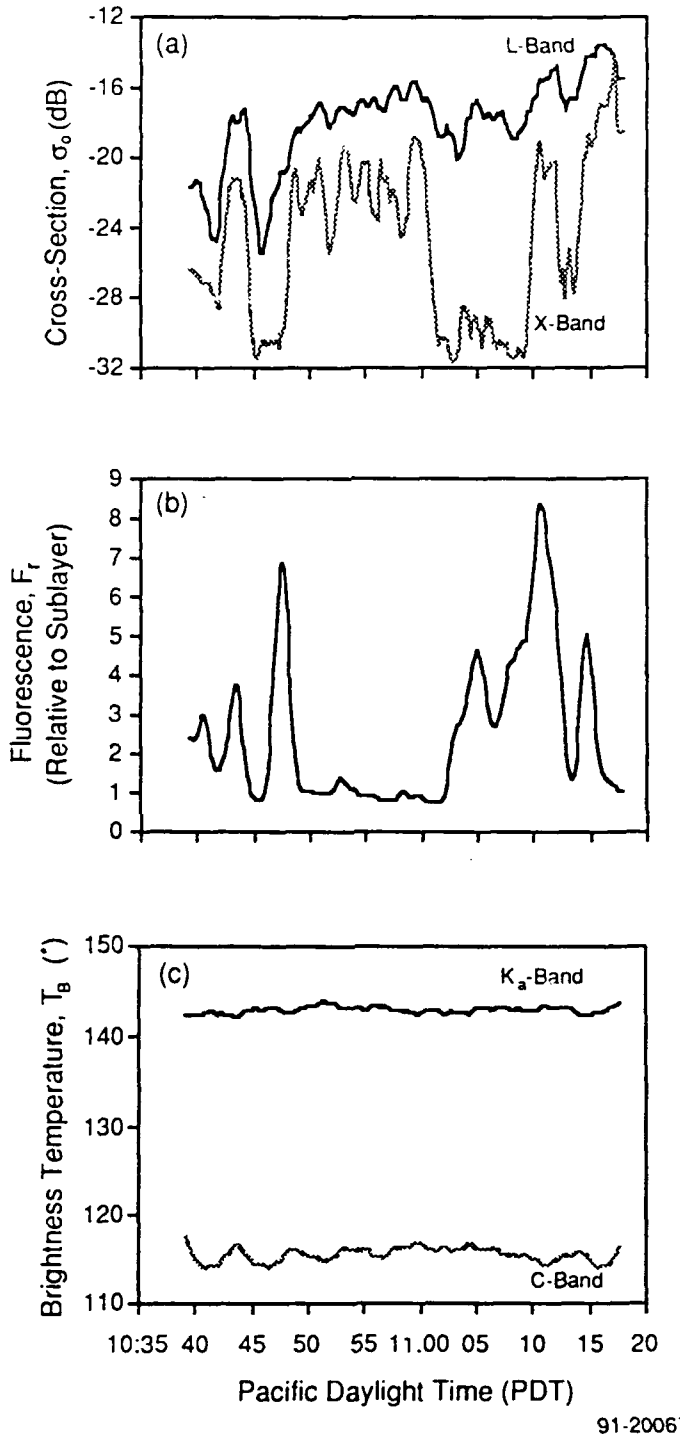

Figure 4. Stacked Plots of Measured Parameters for the 40 Minute Period 10:40 to 11:20 PDT for Two Slick Wave Groups from R/V Wecoma, Morning of October 16, 1989. The Measured Parameters are: (a) Radar Backscatter Cross-Section (σ°), (b) Slick Fluorescence Relative to the Sub-Layer (F_r) and (c) Radiometric Brightness Temperature (T_B). The Polarization was Vertical for the Radiometer and Horizontal Transmit and Horizontal Receive for the Radar Both at an Incidence Angle of $\theta = 25^\circ$.

surfactant microlayer has been corrected. The delay due to the spatial separation of the microwave instruments and the catamaran, $\leq$ 20 sec, has not been corrected. The radiometric brightness temperatures at C-band and Ka-band show no discernible change across the slick bands. That is, any surface slope decrease due to the slicks was not detected by these radiometers.

The UV absorbance and the fluorescence show similar variations across the two surface slick groups of October 16. We select the fluorescence for detailed analysis in the present work. The fluorescence changes from 10:40 to 11:20 is a measure of the concentration of the chlorophyll A within the two slick groups separated by a relatively surfactant free region. The first group is designated as group "A" and the second group is designated as group "B". The three peaks in fluorescence F_r within each slick group are interpreted as three slick bands.

The relative fluorescence F_r increased to a peak value of 7 within the slick group "A" near 10:47. The radar cross-section also decreased about 10 dB at X-band and 6 dB at L-band, both near 10:47, co-located with the fluorescence peak. This co-location is direct evidence that the short Bragg waves are damped at the peak surfactant concentration near the center of the slick band.

The relative fluorescence F_r increased to a peak value of 8 within slick group "B" near 11:10. Different radar cross-section decreases are apparent within slick group "B" compared to slick group "A". The radar cross-section decreased about 10 dB at X-band similiar to slick group "A" whereas the cross section decreased about 2 dB at L-band in contrast to the 6 dB decrease in slick group "A". Furthermore, the X-band decrease occurred over a longer interval, about 8 min, than group "A". This large damping at X-band, reducing the backscattered energy to near the noise floor of the scatterometer, does not allow co-location of the peak fluorescence F_r with the radar minima signatures. That is, this X-band damping occurred across several slick bands within Group "B", whereas, the L-band radar minima are approximately co-located with all three fluorescence peaks.

The wind speed changed from about 1.5 m/s to about 4 m/s while the wind direction changed from about 60° to about 30° with respect to the radar look direction from group "A" to group "B". The wind was blowing generally toward the south and south-east toward the radar look direction. The ship speed was about 0.5 m/s. The wind speeds were light, 1.5-3 m/s

inside group "A" at a wind direction of about 60°. Slightly higher wind speeds, 3-4 m/s were observed inside group "B" at a direction of about 30°. The differences between the X-band radar cross section decreases within the two slick groups could be due to the wind direction changes between the two slick groups. These differences are discussed in more detail in the following sections. Decreases in radar cross section co-located with fluorescence peaks were also observed within several other slicks.

4.0 BRAGG SCATTERING MODEL

Typical ocean remote sensing radars operate at microwave wavelengths in the centimeter or decimeter range at incidence angles, θ from 20-70° within which the radar backscatter is dominated by Bragg scattering. The radar cross-section to first order for horizontal transmit and receive polarization is given by [Valenzuela, 1978],

$$\sigma^0(k_b) = 4\, k_0^4 \cos^4\theta\, |g_{HH}(\theta)|^2\, S(k_b, 0) \qquad (1)$$

where k_0 is the radar wavenumber, $S(k_x, k_y)$ is the spectral density of the ocean surface waves in rectangular coordinates, and $g_{HH}(\theta)$ is the first order scattering coefficient dependent on the relative dielectric constant ϵ_r of the scattering surface,

$$g_{HH}(\theta) = (\epsilon_r - 1)[\cos\theta + (\epsilon_r - \sin\theta)^{1/2}]^{-2} \qquad (2)$$

the coordinate system is chosen such that the k_x is in the same plane as the radar antenna look direction and the internal wave travel direction. Equation (1) can then be used to estimate the ocean wave spectral density at the Bragg wavenumber, k_b, using

$$k_b = 2\, k_0 \sin\theta \qquad (3)$$

Indeed, the cross-section measurements show decreases up to 6 dB and 10 dB at L-band and X-band due to damping of the wave spectral energy at the Bragg wavelengths within the slicks. The Bragg wavenumbers and wavelengths based on the radar configuration used during the October 16 morning measurements are given in Table 2. The radar cross-section is proportional to the ocean wave spectral density at Bragg wavelengths 24 cm (L-band) and 4 cm (X-band). The relative attenuation of 24 cm waves compared to 4 cm waves can be estimated by forming the ratio of the L-band cross-section $\sigma_L^0(k_b)$ to the X-band cross-section $\sigma_X^0(k_b)$ as,

$$\sigma^0(k_{bL})/\sigma^0(k_{bX}) = |g^L_{HH}(\theta)|^2\, S(k_{bL}, 0)/|g^X_{HH}(\theta)|^2\, S(k_{bX}, 0) \qquad (4)$$

It can be shown that the ratio $|g^L_{HH}(\theta)|^2 / |g^X_{HH}(\theta)|^2 \approx 1$ when the imaginary

TABLE 2. BRAGG WAVELENGTH FOR L-BAND AND X-BAND RADAR AT $\theta = 25°$

	L-BAND	X-BAND
k_o	0.314 rad/cm	1.96 rad/cm
k_b	0.26 rad/cm	1.7 rad/cm
λ_b	23.7 cm	3.8 cm
ω_b §	16 rad/s	40 rad/s
f_b	2.5 Hz	6.4 Hz

§ ω_b is the intrinsic angular frequency of the Bragg wave.

part of ϵ_r, $\mathrm{Im}|\epsilon_r| \gg 1$. We contend that this approximation applies to the surfactant free and surfactant covered ocean when $\theta = 25°$ based on $\epsilon_r \approx 73 - 85i$ (L-band) and $\epsilon_r \approx 48 - 35i$ (X-band). That is, the skin depth (electromagnetic penetration depth) is large compared to the surfactant microlayer thickness. Indeed, the skin depth of sea water is about 1 cm and 0.2 cm at L-band and X-band, respectively, whereas the surfactant microlayer thickness is considered less than 0.1 cm. Therefore the scattering coefficient $g_{HH}(\theta)$ should not be substantially effected by this microlayer film. Based on this result, we approximate equation (4) by,

$$\sigma^0(k_{bL})/\sigma^0(k_{bX}) \approx S(k_{bL},0)/\ S(k_{bX},0) \tag{5}$$

The straining of the short Bragg waves by the internal waves can also be inferred using Bragg scattering theory. The normalized differential cross-section $\delta\sigma^0/\sigma^0$ is proportional to the product of the internal wave horizontal-surface strain rate du/dx and the relaxation time τ_r [Alpers, 1985], given by,

$$\delta\sigma^0/\sigma^0 = -(4+\gamma)\ \tau_r\ du/dx \tag{6}$$

where γ is the ratio between the group and phase velocities (0.5 for gravity waves) of the Bragg wave. The relaxation time depends on the radar look direction relative to the wind speed and direction, whereas the strain rate is dependent on the internal wave propagation direction and associated surface current gradient also relative to the radar look direction. The relaxation time is approximately equal to the reciprocal wind wave growth rate when the wind and waves are traveling in the same direction [Plant, 1982] ,

$$\tau_r = \beta^{-1} \approx 25\ (u_*/c)^{-2}\ /\ \omega \tag{7}$$

where u_* is the friction velocity (about 1/25 of the wind speed at 10 m height), c is the phase velocity and ω is the angular frequency of the surface waves. Equation (7) is ,to first order, valid for a clean surface as demonstrated by Plant and a surfactant surface as demonstrated by Mitsuyasu and Honda [1986]. Alpers [1985] has estimated $\tau_r \approx 39$ sec for L-

band Bragg waves at a wind speed of 4 m/s and internal wave strain rates in coastal regions of $du/dx \approx 10^{-3}$ sec^{-1}. However, the relaxation times based on equation (7) are much smaller at shorter wavelengths, $\tau_r \approx 1.6$ sec at X-band (4 cm) for similiar wind speeds. Therefore the predicted changes in the surfactant free surface spectrum at 4 cm wavelengths is a factor of ~25 less than the L-band modulation (24 cm). The above parameters give,

$$\delta\sigma^0/\sigma^0 \sim 18\ \%\quad \text{at L-band} \tag{8}$$

$$\delta\sigma^0/\sigma^0 \sim 0.7\ \%\quad \text{at X-band.} \tag{9}$$

Indeed, the cross-sectional modulation due to straining of the short waves is significantly smaller at X-band than L-band backscatter. More importantly, the radar signature due to straining has been observed as a series of bright and dark bands in radar imagery.

Equations (1) and (5) provide a method of extracting the damping of 24 cm and 4 cm ocean surface waves and their differential damping within a slick band. In contrast. equation (6) gives a method of extracting the product of the surface straining rate and the relaxation time. Furthermore, equation (6) is consistent with the bright/dark bands observed in radar imagery due to change in sign of du/dx. These expressions, equations (1) and (6), can be used to distinguish between cross-sectional radar modulation due to short wave damping and straining.

5.0 DISCUSSION

We investigate the slick related parameters for the period 10:40-11:20 on October 16 in more detail. Stacked plots of selected parameters in Figure 5 are displayed in a format similiar to Figure 4. The cross-section in Figure 5 (a) is given in linear units, rather than logarithmic (dB) units, $\sigma^0_{dB}(k_b)$ = 10 log $\sigma^0(k_b)$. The ratio of the L-band to X-band cross-section is given in Figures 5 (b). The cross-sectional ratio is directly related to the ratio of the spectral densities at the 24 and 4 cm wavelengths, $S(k_{bL},0)/ S(k_{bX},0)$, see equation (5). The relative fluorescence F_r, originally displayed in Figure 4 (c) is also given in Figure 5.

These limited measurements of surface slicks show several interesting features. The relative fluorescence F_r is directly related to the concentration of the chlorophyll A within the slick bands. The ratio of 24 cm spectral damping to 4 cm damping is the largest within slick group "B". We investigate why the L-band cross-section shows a greater backscatter decrease within group "A" compared to group "B". The wind direction changed from 60° relative to the radar look direction in group "A" to 30° in group "B", whereas, the wind speed increased about 1.5 m/s from about 2 m/s to about 3.5 m/s from group "A" to group "B". The individual slick band orientations are considered constant relative to the radar within the two slick groups. The sea surface temperature measured at 15 cm depth increased about 0.1° C from 18.8°C to 18.9°C between group "A" and group "B".

One could argue that the L-band backscatter (24 cm waves) might be more sensitive to the 1.5 m/s wind speed increase than the X-band backscatter (4 cm waves). However, this is unlikely since 4 cm waves respond to wind speed changes more rapidly than 24 cm waves. A more likely explanation is that the L-band backscatter is more sensitive to the wind direction change than the X-band backscatter. That is, the horizontally polarized Bragg scattering angular wind dependence is more sensitive to 24 cm waves than 4 cm waves. We expect the largest damping when the wind in blowing along the radar look direction for X-band
(4 cm).

The largest values of relative fluorescence ($F_r \approx 7$) near 10:47 and 11:10 are approximately co-located with the minimum values in the cross-section for both L-band (24 cm waves) and X-band (4 cm waves). However, some of the locations of the individual slicks do not exactly coincide

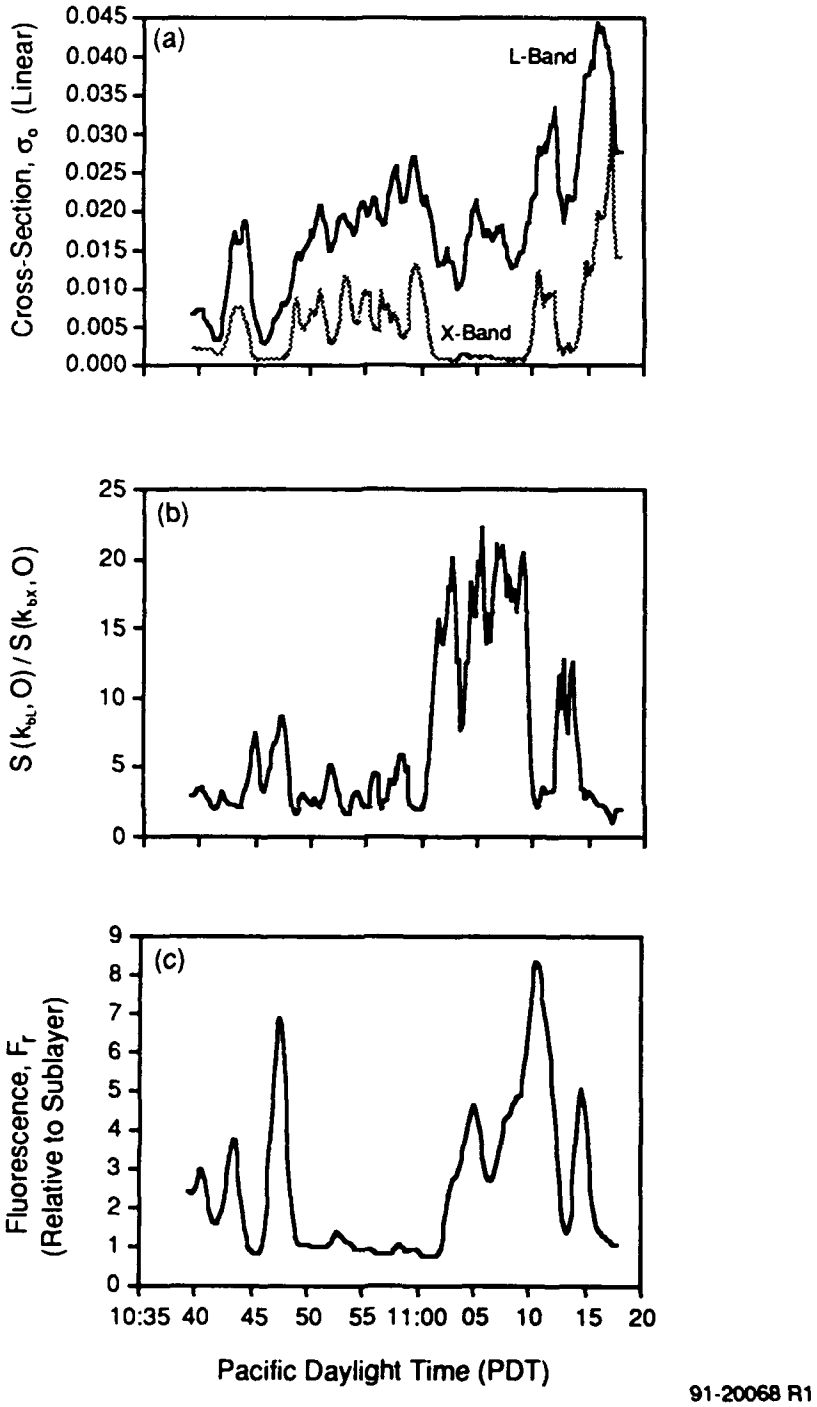

Figure 5. Stacked Plots of Measured Parameters for the 40 Minute Period 10:40 to 11:20 PDT for Similar to Figure 4. The Measured Parameters are: (a) Radar Backscatter Cross-Section (σ°) in Linear Units, (b) Ratio of the L-Band to X-Band Cross-Section, (c) Relative Fluorescence F_r.

with the cross-section decreases. We do not investigate these location discrepancies further in the present work.

The slick characterization as a function of changing wind speed and/or direction is of interest. A considerable amount of radar imagery of surface slicks has been acquired in recent years. However, these synthetic aperture radar (SAR) images are instantaneous two-dimensional snapshot of the slicks, an example is given in Figure 6. That is, changes in cross-section as a function of wind speed or direction are difficult to determine using SAR imagery. Ship-board X-band radar modulations have been reported similiar to aircraft X-band SAR measurements when internal waves travel near the range direction of the radars; see, [Shuchman et al., 1988]. However; for other directions smaller image modulations were observed. Indeed, the lack of bright/dark type radar signatures in the present measurements could possibly be due to the orientation of the slicks relative to the radar look direction or alternately, slicks not associated with internal waves. We expect the maximum bright/dark signature when the slick groups are traveling in the same direction as the radar look direction. The cross-sectional modulation due to straining of the short waves at L-band is in reasonable agreement with the Bragg scattering theory. However, theory predicts, that the X-band modulation is typically a factor of ~ 25 smaller , see equations (8) and (9). Observed radar image modulations show similiar modulations at both L-band and X-band; see, e. g., Lyzenga and Bennett [1988].

The dissipation of wind driven short waves is significantly smaller for the surfactant free sea than within a slick. The surface, instead of being free, is to a first approximation represented by an inextensible (incompressible) microlayer within the slick. This is equivalent to the horizontal velocity of the particles vanishing at the interface between the microlayer and the sea water sub-layer with the vertical gradient of the velocity directly related to the losses due to viscosity at the interface. The wind input to a surfactant free sea must be sufficient to overcome the wind speed threshold which dependents on bulk viscosity of the sea. This threshold is about 1 m/s which means these short waves are essentially always present on the open ocean. The exponential decay time due to the viscosity, τ, of the short gravity waves based on a surfactant free surface (constant surface tension) is,

$$\tau \approx \lambda_b^2/8\pi^2\nu \qquad \text{(clean surface)} \qquad (10)$$

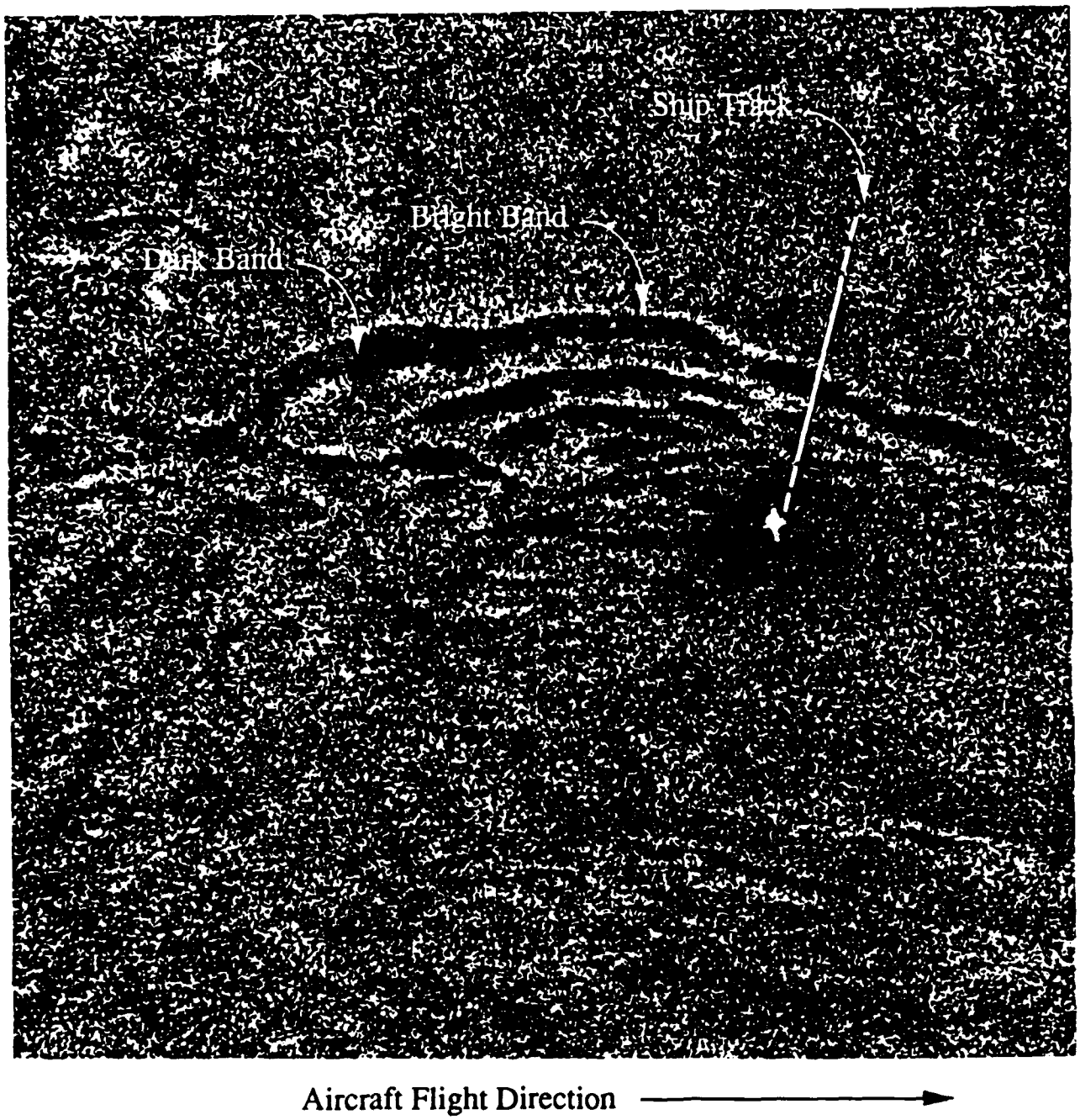

Figure 6. Synthetic Aperture Radar Image of Internal Wave Slicks in the Georgia Straits. This L-Band Radar Image Shows Long Bright and Dark Bands Induced by a Group of Internal Waves Traveling Toward the Top of the Image. The Bright Return Near the Rear of the Wave Group is a Ship.

where the spectral density of the short waves decreases as $\exp(-2t/\tau)$, ν is the kinematic viscosity for sea water, $\nu = 1.78 \times 10^{-2}$ cm^2 s^{-1} then $\tau \approx 0.712\ \lambda_B^2$ where the Bragg wavelength λ_b is given in centimeters. We obtain for the 4 cm and 24 cm waves, $\tau_{f24} \approx 400$ s, $\tau_{f4} \approx 10$ s which indicates that the shorter (4 cm) gravity waves are more rapidly damped (shorter decay time) than the 24 cm waves. However, these waves are continuously generated by the wind input. Therefore both the 4 and 24 cm waves are always present even for light winds.

The viscous damping within slicks is much larger. We consider for the moment that the short waves as generated in adjacent surfactant free regions next to the slicks and propagated into the slick region where they are rapidly attenuated resulting in the cross-section decreases as shown in Figures (4), (5) and (6). The exponential decay time, τ_f, for the short waves within a slick where large concentrations of organic material are present is approximated by an inextensible microlayer as given by Lamb [1932],

$$\tau_f \approx (8/\nu\omega_b k_b^2)^{1/2} \qquad \text{(inextensible microlayer)} \qquad (11)$$

The decay time for short gravity waves are then given by, $\tau_f \approx 0.375\ \lambda_b^{5/4}$ based on deep water dispersion where λ_b is given in centimeters. The shorter wavelengths are damped more strongly than the longer wavelengths, $(\lambda_{bL}/\lambda_{bX})^{5/4} = 9.86$. However, the wind input must also be considered before the radar extracted damping can be compared with equation (11).

Applying equation (11) to the 24 cm and 4 cm waves, we obtain, $\tau_{f24} \approx 20$ s, $\tau_{f4} \approx 2$ s. The viscous decay time for both the free surface and the inextensible microlayer as a function of Bragg wavelength is given in Figure 7. We have assumed for the moment that no short waves are generated within the slick. Therefore, the distance the short waves propagate into an inextensible microlayer depends on the group velocity of the short gravity waves, about 6 m for 24 cm waves and about 0.2 m for 4 cm waves. This idealized model is based on a slick which changes abruptly from a surfactant free region to an inextensible microlayer with wave reflection at the boundary neglected. However, the wind input inside slicks is required before a realistic representation of the waves inside the slick bands can be modeled. Investigation of this wind input is beyond the scope of the present work. A realistic representation of the damping must also take into account the concentration. Intuitively, a slick should approach

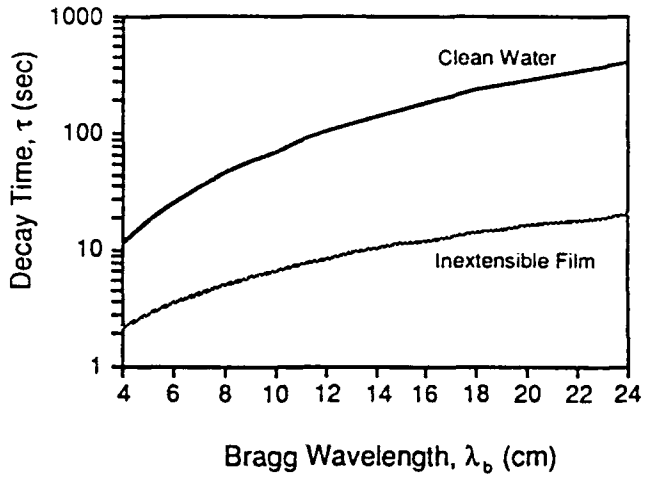

Figure 7. The Exponential Decay Time for Both the Free Surface and the Inextensible Microlayer as a Function of Bragg Wavelength Between 4 cm and 24 cm.

an inextensible microlayer only near it's center with a transition to a relatively surfactant free surface with distance away from the center. The microlayer is essentially elastic in this transition region.

6.0 SUMMARY

The limited measurements reported here show that the peaks in fluorescence, related to the peak concentration of Chlorophyll A, are co-located with the damping of the short gravity waves at both 4 cm and 24 cm wavelengths. The maximum damping ratio between the 24 cm and 4 cm waves is at least 16 for a wind direction of about 30° with respect to the radar look direction and wind speeds, 3-4 m/s.

Imaging-radar slick signatures displaying narrow bright bands on the leading edge of a series of wider dark slick bands have been interpreted as due to short wave straining by internal waves. We assert that the wide dark bands following these bright bands, when observed, are due primarily due to wave damping. That is, these dark bands are related to concentration of the marine surface microlayer material. Therefore, the radar roughness of slicks are related to both short wave damping and wave straining of the short gravity waves.

7.0 REFERENCES

Alpers, W. R., "Theory of Radar Imaging of Internal Waves," Nature 314 (6008), 245-247, 1985.

Apel, J. R. and F. I. Gonzalez, "Non-linear Features of internal waves off Baja California as Observed from the SEASAT Imaging Radar," J. Geophys. Res., 88, 4459-4466, 1983.

Carlson, D. J., "Surface Microlayer Phenolic Enrichment Indicates Sea Surface Slick," Nature, 296, 426-429, 1982.

Carlson, D. J., "Viscosity of Sea-Surface Slicks," Nature, 329, 823-825, 1987.

Carlson, D. J., J. L. Cantey and J. J. Cullen, "Description of and Results From a New Surface Microlayer Sampling Device," Deep Sea Res., 35(7), 1205-1213, 1988.

Ewing, G., "Slicks, Surface and Internal Waves," J. Mar. Res., 9(3), 161-187, 1950.

Gasparovic, R. F., J. R. Apel and E. S. Kasischke, "An Overview of the SAR Internal Wave Signature Experiment," J. Geophys. Res., 93(C10), 12, 304-12, 316, 1988.

Hühnerfuss, H., and Alpers, W., "Molecular Aspects of the System Water/Monomolecular Surface Film and the Occurrence of a New Anomalous Dispersion Regime at 1.43 GHz," J. Phys. Chem., 87, 5251-5258, 1983.

LaFond, E. C., "Internal Waves, in the Sea," vol 1, M. N. Hill (Ed.), Interscience Publishers, New York, 1962.

Levich, V. G., "Physicochemical Hydrodynamics," Prentice Hall, Inc., Englewood Cliffs, N. J., 1962.

Lamb, H., "Hydrodynamics," Dover Publications Inc., New York, pp 623-632, 1932.

Lyzenga, D. R., and Bennett, J. R., "Full Spectrum Modeling of Synthetic Aperture Radar Internal Wave Signatures," J. Geophys. Res. 93, 12, 345-12, 354, 1988.

Mitsuyasu, H., and Honda, T., "The Effects of Surfactant on Certain Air-Sea Interaction Phenomena," in Wave Dynamics and Radio Probing of the Ocean Surface (Ed., O. M. Phillips and K. Hasselmann) Plenum Press, New York, 1986.

Plant, W. J., "A Relationship between Wind Stress and Wave Slope," J. Geophys. Res. 87(C3), 1961-1967, 1992.

Rufenach, C. L., and Smith, C., "Observation of Internal Waves in LANDSAT and SEASAT Satellite Imagery," Int. J. Remote Sensing, 6, 1201-1207, 1985.

7.0 REFERENCES (Concluded)

Shuchman, R. A., Lyzenga, D. R., Lake, B. M., Hughes, B. A., Gasparovic, R. F., and Kasischke, E. S., "Comparison of Joint Canada-U.S. Ocean Wave Investigation Project Synthetic Aperture Radar Data With Internal Wave Observations and Modeling Results," J. Geophys. Res. 93, 12,283-12,291, 1988.

Valenzuela, G. R., Theories for the Interaction of Electromagnetic and Oceanic Waves - A review, Boundary Layer Meteorol. 13, 61-85, 1978.

ON THE FEASIBILITY OF MEASURING SEA SURFACE TEMPERATURE USING ACTIVE AND PASSIVE MICROWAVE SENSORS

Clifford L. Rufenach and Robert A. Shuchman
Environmental Research Institute of Michigan
Ann Arbor, Michigan

September 18, 1991

Accepted for publication in the International Journal of Remote Sensing

ABSTRACT

We study the feasibility of using a dual linear-polarized radiometer operating at 6 GHz in conjunction with a scatterometer as a method of extracting sea surface temperature. A model originally developed by Wilheit [1979] is used to investigate the sensitivity of radiometric temperature to changes in wind speed, U, at a height of 20 m; that is, the accuracy of sea temperature depends directly on the accuracy of radiometric temperature. These changes are corrected using this extracted wind speed based on a scatterometer wind accuracy of ± 1 m/s. We show that a vertically polarized radiometer is less sensitive to wind speed changes than a horizontally polarized one near an incidence angle $\theta = 60°$. Furthermore, we quantify the wind variation; $\Delta T_B^V/\Delta U \leq 0.12°C/m/s$ when $U > 10$ m/s and $\Delta T_B^H/\Delta U \leq 2.0°C/m/s$ when $U > 6$ m/s for vertical and horizontal polarization, respectively. Thus, the resulting error is ± 0.12°C and ± 2.0°C for T_B^V and T_B^H, respectively. These results suggest that a scatterometer can be used to correct the wind speed dependence of a vertically polarized radiometer operating near 6 GHz using a pencil antenna beam pointing at an incidence angle near 57°.

1.0 INTRODUCTION

Extraction of sea surface temperature using passive microwave radiometric measurements in conjunction with microwave scatterometer measurements is a technique which has not been exploited. The technique uses the scatterometer extracted surface wind speed to correct the wind dependence of the radiometric brightness temperature. The accuracy achieved depends on the accuracy of the radiometric brightness temperature measurement itself, the accuracy of associated models, and the accuracy of the extracted wind speed based on the scatterometer measurements.

The radiometric temperature of an ocean surface depends primarily upon its sea surface temperature, salinity, surface wind speed (surface roughness), and foam cover. The radiometric temperature of a smooth surface does not depend on the wind speed or foam cover. More precisely, foam cover is not important for wind speeds less than about 7 m/s. The wind speed U is referenced to a height of 20 m since most surface measurements have been acquired at this height. The radiometric temperature of a smooth sea surface depends on sea surface temperature and salinity. This dependence is known accurately through its relationship with the complex dielectric constant of sea water [Klein and Swift, 1977]. The surface wind influences the radiometric temperature through the ocean wave spectrum. However, measurements are not fully consistent with each other or with the theory especially when foam is present [Hollinger, 1971; Monahan and O'Muircheartaigh, 1980; Smith, 1988].

This study is limited to determining an optimum radiometric frequency for active/passive sensor system and the investigation of the emissivity dependence on wind speed. The model examined depends on atmospheric and ocean parameters discussed above. However, it does not include a discussion of radiometric measurements usually taken near 18 and 37 Ghz to correct for water vapor and clouds which are most important at aircraft and spacecraft altitudes [Guissard and Sobieski, 1987].

2.0 MODELS

The radiometric temperature T_B for a near surface down-looking radiometer over a rough half space (wind sea) based on thermodynamic equilibrium is related to the sea surface temperature T_S (in °K) by,

$$T_B = e(S, U, T_S) T_S \tag{1}$$

where S is the salinity of the ocean, U is the wind speed at 20 m, e is the emissivity of the rough ocean, and $T_S(°C) = T_S(°K) - 273.16$. The emissivity for a smooth sea at normal incidence is given by,

$$e_s = 1 - \left| \frac{1-\sqrt{\epsilon}}{1+\sqrt{\epsilon}} \right|^2 \tag{2}$$

where ϵ is the complex dielectric constant of sea water.

The dielectric constant ϵ of sea water is dependent on the ionic conductivity σ in mhos/m, relaxation constant τ in sec., and static dielectric constant ϵ_s [Debye, 1929] as given by,

$$\epsilon = \epsilon_\infty + \frac{\epsilon_S - \epsilon_\infty}{1 + (j\omega\tau)^{1-\alpha}} - j\frac{\sigma}{\omega\epsilon_0} \tag{3}$$

where $\epsilon_0 = 8.854 \times 10^{-12}$ is the permittivity of free space in farads/m, ϵ_∞ is the permittivity at a high frequency, $\omega = 2\pi f$ is the microwave radian frequency with f in Hz, α is an empirical constant and σ, τ, and ϵ are all functions of S and T_S. Empirical values of σ, τ, and ϵ as a function of S and T_S were given by Klein and Swift [1977] for the microwave frequencies 1.43 and 2.65 GHz. We use these empirical values to investigate a suitable radiometric frequency for which the emissivity dependence on salinity is negligible, see section III. The selection of this frequency allows the simplification of equation (1) resulting in T_B depending on only U and T_S,

$$T_B = e(U, T_S) T_S \, . \tag{4}$$

We now, in principle, can extract the wind speed U and surface temperate T_S using

equation (4) and,

$$U = f^{-1}(\sigma_0) \tag{5}$$

where σ_o is the scatterometer backscattering cross-section and f^{-1} is the inverse of the function f given by,

$$\sigma_0 = f(U) = aU^b \tag{6}$$

where a and b are empirical constants dependent on the scatterometer frequency and the wind direction. The extracted winds at 20 m are accurate to about $\pm$ 1 m/s based on aircraft circle flights, upwind, crosswind and downwind; see, e. g., Donelan and Pierson [1987].

The emissivity dependence on U and T_s, given in equation (4), has been modeled quantitatively by Wilheit [1979]. This numerical model originally developed by Stogryn [1967] has been simplified by Wilheit based on an isotropic normal distribution for the ocean wave slopes. Wilheit obtained good agreement between the model and radiometer measurements based on this simplification with the variance of the slope increasing linearly with the radiometric frequency. Furthermore, for high wind speeds, he also included the effect of foam on the radiometric temperature. He treated foam as partially obscuring the surface independent of polarization. Equation (4) and this model are used to estimate the emissivity dependence on U and T_s.

3.0 RESULTS

The optimum radiometric frequency is selected such that both the emissivity dependence on salinity is negligible and the atmospheric effects due to water vapor and clouds are minimized. This results in the lowest frequency consistent with negligible dependence on salinity. Blume et al.[1978] used radiometers operating at 1.43 and 2.65 GHz to measure salinity with aircraft flights over an estuary. Since both of these frequencies are sensitive to salinity, an optimum frequency must be larger than 2.65 GHz. We use equations (2) and (3) and Klein and Swift's results in the range $3 < f < 10$ GHz to investigate the minimum frequency which results in an error in radiometric temperature of less than 0.04°C per ppt in salinity. The salinity of surface water remains relatively constant for long periods of time (near 34.6 ppt) with a geographic latitude variation of about 1 ppt provided specific areas are excluded. These areas include coastal regions, especially estuaries and melting ice in polar regions [Williams, 1962].

The results of our investigation are shown in Figure 1 (a) with the emissivity as a function of T_S with an optimum frequency of 6 GHz; while, Figure 1 (b) illustrates the same variation at 2.65 GHz for comparison. The range of salinity was varied from 20 ppt to 40 ppt in intervals of 2 ppt. Each ppt interval change in Figure 1 (a) corresponds to ≤ 0.00013 change in emissivity or equivalently ≤ 0.038°C/ppt. Each ppt interval in Figure 1 (b) corresponds to ≤ 0.0007 or ≤ 0.22°C/ppt. These results are based on $T_S \leq 20$°C. Therefore the optimum radiometric frequency is near 6 GHz as given in Table 2(a). Indeed, a typical salinity change of 1 ppt with latitude causes a change in T_S of 0.038°C at C-band (6 GHz) and 0.22°C at S-band (2.65 GHz) at normal incidence.

We now consider the emissivity dependence on only U and T_S using equation (4) and Wilheit's model. The variation of the emissivity with incidence angle for three wind speeds, U = 6, 10 and 20 m/s are given in Figure 2 (a). Wind speeds less than 6 m/s have negligible foam cover. The upper three curves correspond to vertical polarization and the lower three curves to horizontal polarization. The vertically polarized curves tend to intersect at an incidence angle θ between 50° and 60°. Therefore these incidence angles correspond to a minimum dependence on wind speed which is the same result as previously reported by Stogryn [1967]. The percent of effective foam cover for wind speeds from 8 to 20 m/s based on the model are given in Table 1. Figure 2 (b) shows the same results as Figure 2 (a) except the differential emissivity is displayed on the vertical axis. This normalized differential emissivity $\delta e/e$, in percent is defined as,

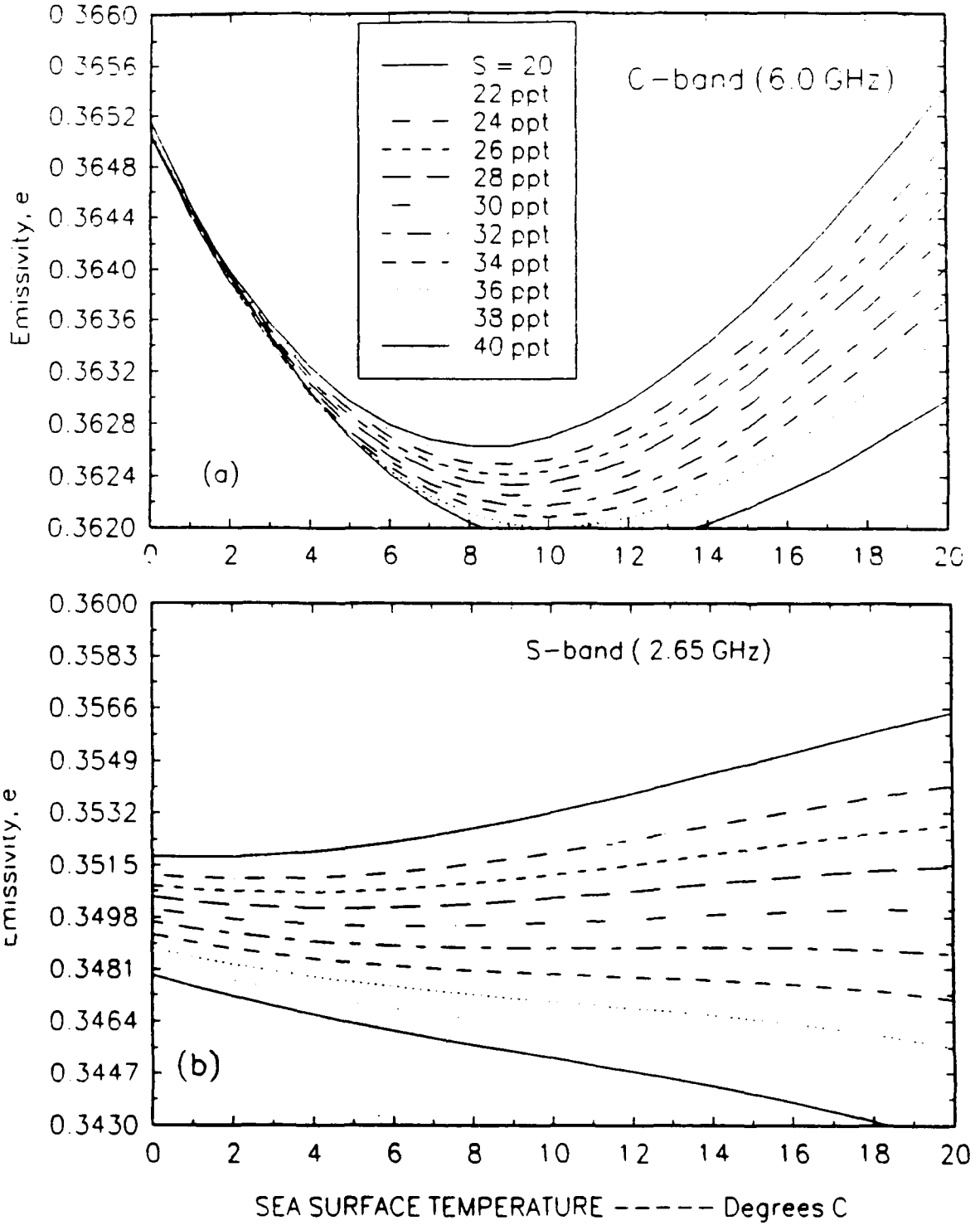

Figure 1. Emissivity Variation with Sea Surface Temperature T_S Based on a Smooth Sea Parameterized in Salinity, S in ppt, at Normal Incidence Using; (a) Radiometric Frequency of 6 GHz (C-Band), and (b) Radiometric Frequency of 2.65 GHz (S-Band).

TABLE 2(a).
Radiometric Brightness Temperature Sensitivity to Salinity at Normal Incidence

	OPERATING FREQUENCY	
	C-BAND (6 GHz)	S-BAND (2.65 GHz)
$\Delta T_B/\Delta S$	0.038°C/ppt	0.22°C/ppt

TABLE 2(b).
Radiometric Brightness Temperature sensitivity to Wind Speed, S = 34 ppt and θ = 60°.

C-BAND (6 GHz)	POLARIZATION	
	VERTICAL	HORIZONTAL
$\Delta T_B/\Delta U$	$\leq$ 0.12°C/m/s	$\leq$ 2.0°C/m/s

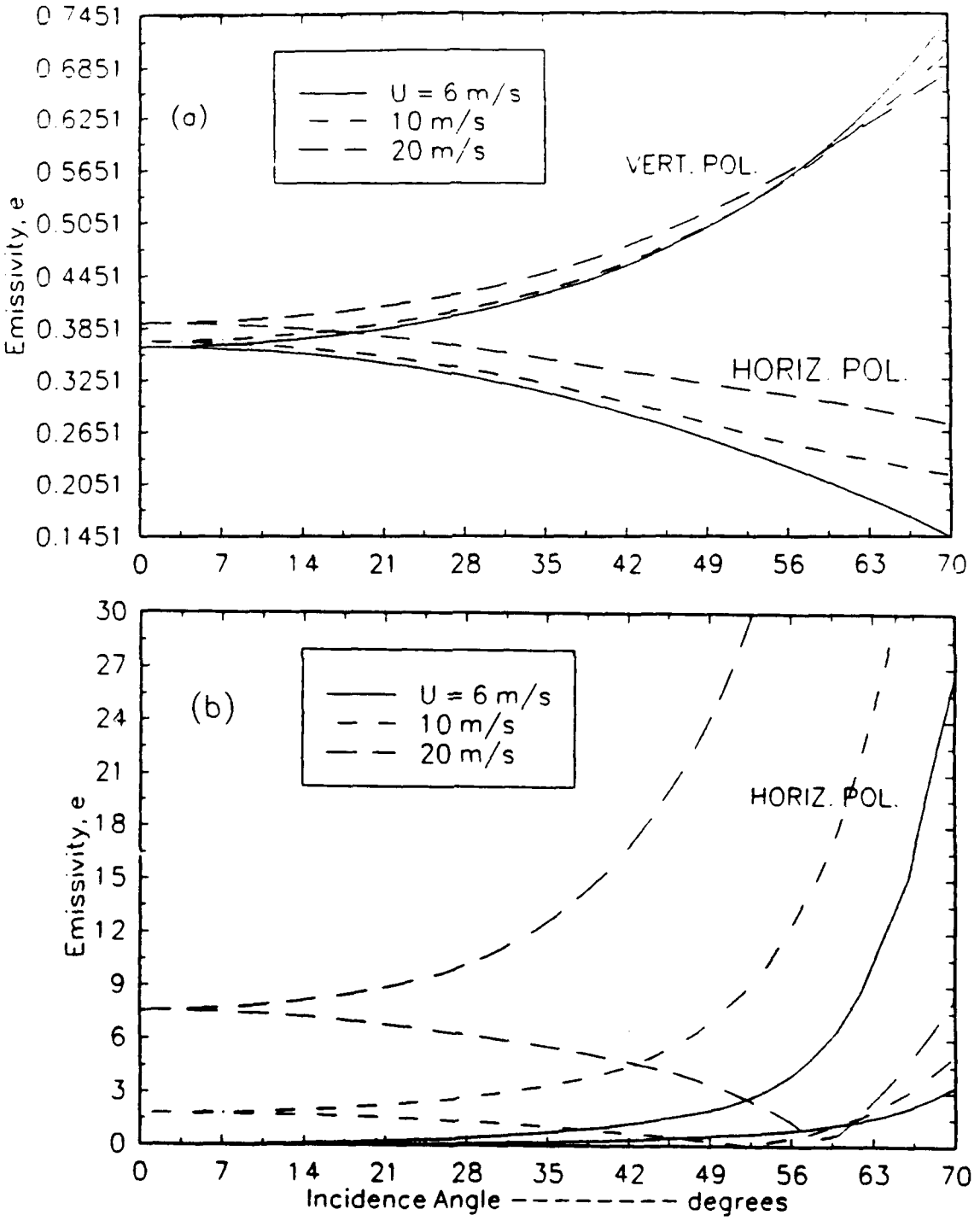

Figure 2. **Emissivity Variation with Incidence Angle θ Parameterized in Surface Wind Speed, U = 6 m/s, 10 m/s and 20 m/s. The Salinity S = 34 ppt and the Sea Surface Temperature T_s = 18°C. The Upper Three Curves Correspond to Vertical Polarization and the Lower Three Curves Correspond to Horizontal Polarization; (a) Emissivity, and (b) Differential Emissivity.**

TABLE 1.

WIND SPEED AND ASSOCIATED PERCENT EFFECTIVE FOAM COVER
BASED ON WILHEIT [1979]

U(m/s)	FOAM(%)
6	0
8	.33
10	.99
12	1.65
14	2.31
16	2.97
18	3.63
20	4.31

$$\frac{\delta e(\theta)}{e_S(\theta)} = 100 \frac{(e_S(\theta) - e(\theta))}{e_S(\theta)} \quad \% \tag{7}$$

where $e_s(\theta)$ is the emissivity of the smooth sea as a function of incidence angle and $e_{sH}(\theta)$ and $e_{sV}(\theta)$ are the corresponding vertical and horizontal polarizations of $e_s(\theta)$ given by,

$$e_{sH}(\theta) = 1 - \left| \frac{\cos\theta - \sqrt{\epsilon - \sin^2\theta}}{\cos\theta + \sqrt{\epsilon - \sin^2\theta}} \right|^2 \tag{8}$$

$$e_{sV}(\theta) = 1 - \left| \frac{\epsilon\cos\theta - \sqrt{\epsilon - \sin^2\theta}}{\epsilon\cos\theta + \sqrt{\epsilon - \sin^2\theta}} \right|^2 \tag{9}$$

The three lower curves correspond to vertical polarization and the three upper curves correspond to horizontal polarization. The differential emissivity for the vertical polarization consistently shows a lower percent variation as a function of incidence angle and wind speed.

We next consider the emissivity dependence on sea surface temperature for a range of wind speeds, U = 6 - 20 m/s at $\theta = 60°$. Figure 3(a) shows the emissivity dependence on U and T_S for horizontal polarization whereas Figure 3 (b) shows this same dependence for vertical polarization. The primary result is that the vertical polarized T_B^V is only weakly dependent on wind speed when 6 m/s $\leq$ U $\leq$ 10 m/s whereas at higher wind speeds the change in emissivity is $\Delta e/\Delta U \leq 0.00042$/m/s or in terms of T_B^V is $\Delta T_B^V/\Delta U \leq 0.12°C$/m/s. In contrast, the change in emissivity for horizontal polarization is $\Delta e/\Delta U \leq 0.007$/m/s or $\Delta T_B^H/\Delta U \leq 2.0°C$/m/s when U > 6 m/s. These T_B sensitivities to wind speed are summarized in Table 2(b). The maximum error is $\pm$ 0.12°C and $\pm$ 2.0°C for T_B^V and T_B^H respectively based on the scatterometer wind accuracy of $\pm$ 1 m/s assuming no errors in the model and the measurement of the T_B^V and T_B^H.

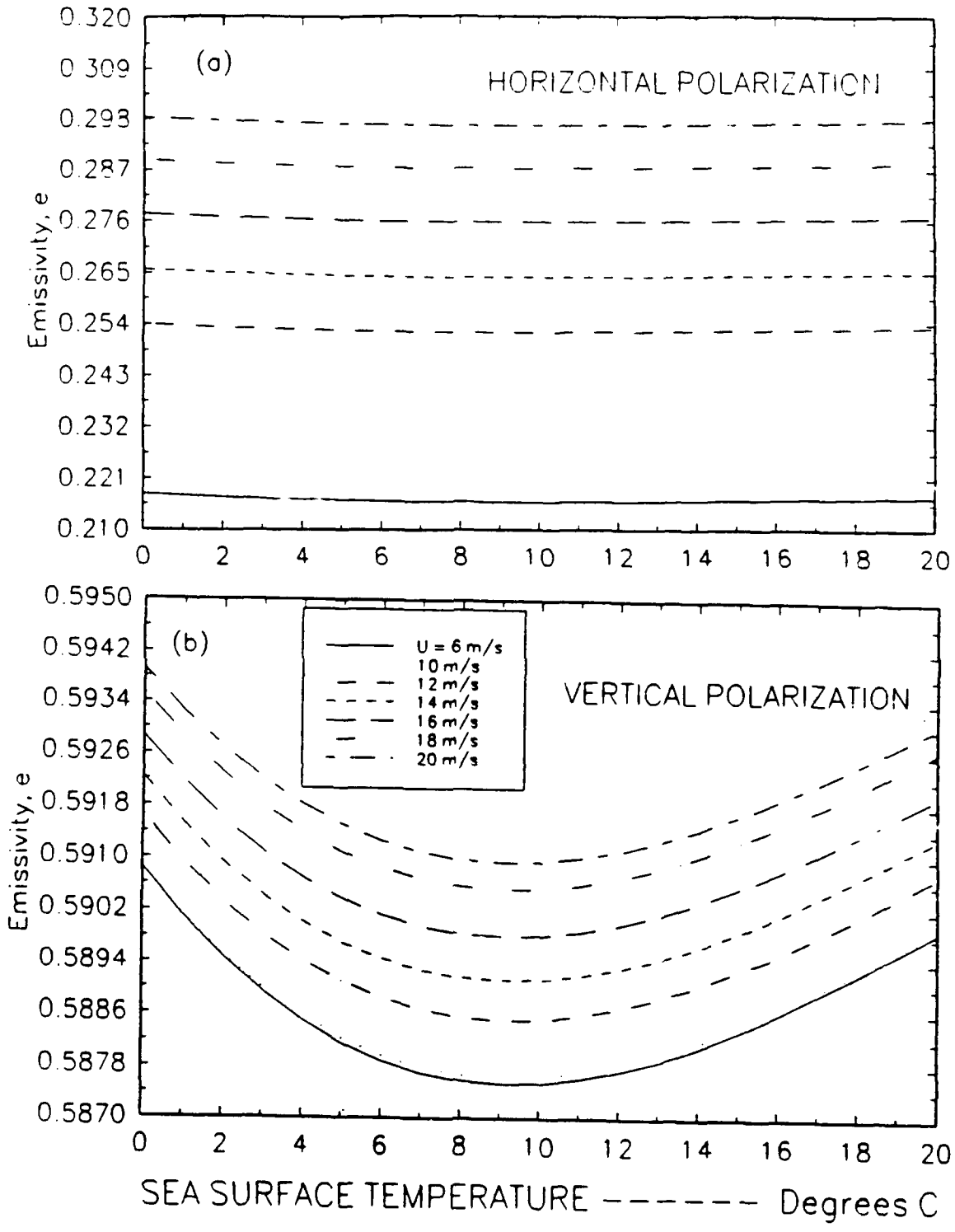

Figure 3. **Emissivity Variation with Sea Surface Temperature T_S Parameterized in Surface Wind Speed, U = 6 - 20 m/s, θ = 60° and Salinity, S = 34 ppt; (a) Horizontal Polarization, and (b) Vertical Polarization.**

4.0 SUMMARY

The model results suggest an experiment using a tower-based radiometer operating at 6 GHz with measurements taken simultaneous at horizontal and vertical polarizations using a pencil beam antenna selected at an incidence angle near 57°. These measurements would be acquired in conjunction with scatterometer and wind anemometer measurements in an area where high winds and ocean temperature fronts frequently occur allowing the validation of the models and the measuring technique.

5.0 ACKNOWLEDGEMENTS

This work is supported by the Office of Naval Research (ONR) under contract N00014-89-C-0117. The technical monitor is Dr. Frank Herr.

6.0 REFERENCES

Blume, H. C., Kendall, B. M., and Fedors, J. C., 1978, "Measurement of Ocean Temperature and Salinity Via Microwave Radiometry". Boundary Layer Met. 13, 295-308.

Debye, P., 1929, "Polar Molecules", (New York: Dover reprint; original Reinhold).

Donelan, M. A., and Pierson, W. J., 1987, "Radar Scattering and Equilibrium Ranges in Wind-Generated Waves with Application to Scatterometry". J. Geophys. Res. 92(C5), 4971-5029.

Guissard, A., and Sobieski, P., 1987, "An Approximate Model for the Microwave Brightness Temperature of the Sea", Int. J. Remote Sensing, 8, 1607-1627.

Hollinger, J. P., 1971, "Passive Microwave Measurements of Sea Surface Roughness". IEEE Trans. Geosci. Elect. GE-9(3), 165-169.

Klein, L. A., and Swift, C. T., 1977, "An Improved Model for the Dielectric Constant of Sea Water at Microwave Frequencies". IEEE Trans. Ant. Prop. AP-25(1), 104-111.

Monahan, E. C., and O'Muircheartaigh, I., 1980, "Optimal Power-Law Description of Oceanic Whitecap Coverage Dependence on Wind Speed", J. Phys. Oceanogr. 10, 2094-2099.

Smith, P. M., 1988, "The Emissivity of Sea Foam at 19 and 37 GHz", IEEE Trans. Antennas Propagat., GE-26, 541-547.

Stogryn, A., 1967, "The Apparent Temperature of the Sea at Microwave Frequencies", IEEE Trans. Ant. Prop. AP-15(2), 278-286.

Wilheit, T., 1979, "A Model for the Microwave Emissivity of the Ocean's Surface as a Function of Wind Speed". IEEE Trans. Geosci. Elect. GE-17(4), 244-249.

Williams, J, 1962, "Oceanography: An Introduction to Marine Science", (Boston: Little, Brown and Co.)